Supporting Information

Recombinant Expression and Chemical Amidation of Isotopically Labeled Native Melittin

Martin D. Gelenter and Ad Bax*
Laboratory of Chemical Physics, NIDDK, National Institutes of Health, Bethesda, MD 20892

* Corresponding author: Ad Bax: bax@nih.gov

1. Detailed Description of the Production of Isotopically Labeled Native Melittin

1.1 Recombinant Expression

1.1.2 Expression of $^{2}H,^{13}C,^{15}N$-Labeled GST-melittin-COOH

The first two constructs we tried to express consisted of the B1 domain of Streptococcal protein G (GB1)[1] (6.2 kDa) or the small ubiquitin-related modifier (SUMO)[2,3] (11 kDa) as the solubility tag. In our hands, neither of these constructs showed overexpression of the fusion protein, most likely due to the fusion partners not being able to inhibit melittin's antimicrobial properties. We then turned to a more established fusion partner for recombinant expression of melittin: glutathione S-transferase (GST).[4–7] The gene encoding melittin-COOH preceded by a flexible linker and TEV cleavage site[8] was synthesized and cloned into the pD454-GST vector (ATUM, Newark, CA). This GST-TEV-melittin-COOH plasmid (**Fig. 1a**) was transformed into BL21-Gold (DE3) competent cells (Agilent, Santa Clara, CA). A 25% glycerol stock solution of cells containing the GST-melittin-COOH plasmid was stored at -80 °C for the innoculation of GST-TEV-melittin-COOH expression cultures.

A 2.5 mL LB preculture supplemented with 1% glucose and 100 μg/mL carbenicillin was innoculated with the glycerol cell stock and incubated at 37 °C and 220 RPM for 7 hours until the optical density at 600 nm (OD_{600}) reached 2.2. A 1 mL volume of the LB preculture was used to innoculated 2×80 mL of DCN M9 media (96-mM Na_2HPO_4, 44-mM KH_2PO_4, 17-mM NaCl, 2-mM $MgSO_4$, 40-μM biotin, 7.5 μM thiamine, 100 μM $CaCl_2$, 100 μg/mL carbenicillin, 10 mL MEM Vitamin Solution (100×) (Thermo Fisher, Waltham, MA), 1.5 g/L 99% ^{15}N-labeled NH_4Cl (Cambridge Isotopes Laboratories, Tewksbury, MA), and 3 g/L 97-98% $^{13}C,^{2}H$-labeled glucose (Cambridge Isotopes Laboratories, Tewksbury, MA) in 99.9% D_2O (Thermo Fisher, Waltham, MA), which was incubated overnight (14 hours) at 37 °C and 220 RPM; the OD_{600} in the morning was 4.0.

Two 1-L DCN M9 media main cultures were innoculated with 80 mL from the starter culture and supplemented with 0.5 g/L ISOGRO-$^{13}C,^{15}N$,D (Millipore Sigma, Burlington, MA) prior to incubation at 37 °C and 220 RPM until the OD600 reached 1.1 (3 hours). At this point, the cultures were moved to a shaker at 18 °C and 150 RPM for one hour before being induced with 150 μM isopropyl β-D-1-thiogalactopyranoside (IPTG) and changing the shaking speed to 190 RPM. The OD_{600} when the cultures were induced was 1.4. After 22 hours of induction the cells were harvested by centrifugation (4500 RPM for 45 minutes) in 1-L HarvestLine System Liners (Beckman Coulter, Indianapolis, IN). The supernatant was decanted and the cell pellets were frozen at -80 °C overnight.

1.1.3 GST affinity column purification of GST-melittin-COOH

The cell pellets containing recombinant $^{2}H,^{13}C,^{15}N$-labelled GST-TEV-melittin-COOH were resuspended in 200 mL Lysis Buffer (phosphate buffer saline (PBS) pH 7.4, 1-mM 1,4-dithiothreitol (DTT), 0.1% Triton-X 100 (Millipore Sigma, St. Louis, MO), 0.2 mg/ml lysozyme, and 3 cOmplete EDTA-free Protease Inhibitor Cocktail tablets (Roche, Mannheim, Germany) and stirred vigorously at room temperature for 15 minutes before being moved to 4 °C for 1.5 hours. The cells were then lysed by probe sonication (30 seconds on, 1 minute off, twenty repeats, to give a total processing time of 10 minutes). The lysate was then stirred vigorously at 4 °C for 2 hours before being spun down at 20,000 RPM for 1 hour.

The cell lysate supernatant was filter sterilized using a 0.22-μm sterile membrane filter before being loaded onto three 5-mL GSTrap HP GST affinity chromatography columns (Cytiva, Marlborough, MA) attached in series for a total column volume of 15 mL at a flow rate of 2 mL/min. The columns were then washed with 200 mL Wash Buffer (PBS (pH 7.4), 1-mM DTT, 0.1% Triton-X 100) at a flow rate of 5 mL/min. The GST-melittin-COOH was eluted from the column with 25 mL of Elution Buffer (50-mM Tris (pH 9.0), 1-mM DTT, 0.1% Triton-X 100, 200-mM NaCl, 10-mM glutathione). There was approximately 75 mg of GST-melittin-COOH fusion protein per L of DCN M9 expression culture (**Fig. S1a**).

1.1.4 TEV Cleavage of GST-melittin-COOH

The GSTrap elution was then dialyzed against 4 L of TEV cleavage buffer (25-mM Tris (pH 7.5), 100-mM NaCl, 0.5-mM EDTA, 1-mM DTT, 0.1% Triton-X 100, and 1-mM benzamidine) overnight at room temperature. The next morning 0.7 mg of TEV protease (expressed and purified in our lab. We thank Dr. John M. Louis for providing us with a glycerol stock containing BL21(DE3) E. coli cells transfected with a plasmid encoding for MBP-TEV with ampicillin and chloramphenicol resistance) was added to the solution to cleave GST from melittin-COOH. The TEV cleavage site leaves the N-terminal glycine intact for melittin-COOH. The extent of cleavage was monitored with SDS-PAGE gels. For the next three days, 0.7 mg aliquots were added to the cleavage reaction in the morning and the evening such that the final cleavage reaction contained 4.3 mg of TEV protease per L of expression media. After four days, nearly complete cleavage was attained.

1.1.5 Separation of GST and TEV from melittin-COOH

The cleavage reaction solution was then loaded onto the GSTrap column equilibrated in Wash Buffer at a flow rate of 3.5 mL/min. The flowthrough contained TEV and melittin-COOH, while GST was retained on the column and later eluted with Elution Buffer. The cleavage reaction was quenched with the addition of acetonitrile and trifluoroacetic acid (TFA) to final concentrations of 20% and 1%, respectively, and the sample was further prepared for reversed-phase high-performance liquid chromatography (HPLC) by a five-fold dilution with MilliQ water. The sample was then loaded onto a Jupiter 4-μm Proteo 90-Å 250 × 10 mm HPLC Column (Phenomenex, Torrance, CA) at a flow rate of 3 mL/min. A gradient of 20%-95% acetonitrile with 0.05% TFA lasting 30 minutes, followed by a 13.3 minute 95% acetonitrile wash was used to elute TEV, melittin-COOH, and the Triton-X 100 that had bound to the column (**Fig. S1b, Fig. S2a**). Melittin-COOH eluted at ~45% acetonitrile. Elution fractions from six HPLC runs were pooled together and lyophilized.

1.2 Chemical Amidation

1.2.1 BOC protection of melittin-COOH

A total of 4.9 mg lyophilized melittin-COOH was dissolved in 3 mL *N,N*-dimethylformamide (DMF) under N_2 atmosphere. Seven molar equivalents of *N,N*-diisopropylethylamine (DIPEA) (1.99 μL) were then added to the solution to deprotonate the N-terminus and basic sidechain residues. Seven molar equivalents of di-*tert*-butyl dicarbonate (Boc_2O) (2.49 mg) were then added to the solution to Boc-protect the N-terminus and lysine side chains (**Fig. 1b**). The reaction was stirred vigorously at room temperature under N_2 atmosphere for 23 hours.

The Boc-protection reaction was quenched by the addition of 5% TFA, 50% H_2O, and 30% acetonitrile to the DMF solution. The reaction mixture was then HPLC purified using an acetonitrile gradient of 50%-95%. Boc-melittin-COOH is very hydrophobic and does not elute until ~90% acetonitrile is reached (**Fig. S2b**). The elution was then lyophilized.

1.2.2 Amidation of Boc-melittin-COOH

A total of 2.7 mg lyophilized Boc-melittin-COOH was dissolved in 1 mL DMF under N_2 atmosphere. Then, 2.7 molar equivalents of DIPEA (0.45 μL) were added to the solution to deprotonate the C-terminal carboxylic acid and to later on deprotonate $^{15}NH_4Cl$.[9] After that, 1.7 molar equivalents of 1-[Bis(dimethylamino)methylene]-1H-1,2,3-triazolo[4,5-b]pyridinium 3-oxide hexafluorophosphate (HATU) (0.64 mg) were added to the solution to activate the C-terminal carboxylic acid into a reactive ester. The solution was stirred vigorously for 10 minutes before 1.7 equivalents of $^{15}NH_4Cl$ (0.09 mg) were added to the reaction. Due to the low solubility of NH_4Cl in DMF, the NH_4Cl was first dissolved in 100 μl DMF by bath sonication at 35 °C for 40 minutes followed by vortexing. The reaction was stirred at room temperature under an N_2 atmosphere for 23 hours. At that point, the solution was dried down to a film with an N_2 stream overnight.

Melittin is devoid of any acidic side chains, which makes the chemical modification of its C-terminal carboxylic acid more straightforward than for peptides or proteins containing aspartic acid (D) or glutamic acid (E) residues. There is a vast number of amidated membrane-lytic, antimicrobial, and hormone peptides that do not contain D or E residues, for which the Boc protection strategy will be directly applicable (**Table S1**).

There are a number of strategies that can be pursued for chemical amidation of a peptide containing D or E. Simplest would be to check whether the higher reactivity of the C-terminal carboxylic acid compared to D or E carboxylic acid side chains can be exploited to kinetically favor the desired product. C-terminal carboxylic acids are more reactive than their D or E sidechain counterparts and are therefore more easily activated and amidated in subsequent reaction steps. To make this strategy more likely to succeed, it would be advised to use less than one molar equivalent of HATU for activation and to add the $^{15}NH_4$ nucleophile at the same time to limit unwanted side reactions. If an excess of the peptide is used to limit side reactions, unreacted peptide can be separated via HPLC and/or ion exchange chromatography and re-reacted to maximize the yield.

If reactions with the C-terminal carboxylic acid in the presence of unprotected D or E side chains is not kinetically favorable enough to attain a reasonable yield of the desired product, a strategy involving orthogonal carboxylic acid protecting groups would be the best avenue to take. This could be done by first selectively protecting the more reactive C-terminus with protecting groups that are removed with low concentrations of TFA, such as 2-chlorotrityl or 2-phenylisopropyl, which can be deprotected with 1% and 4% TFA, respectively.[10] Following this protection step and a work-up to isolate the C-terminally protected peptide, the D or E side chains can be protected with a *tert*-butyl group, which typically requires deprotection in 90% TFA.[10] The C-terminal protecting group can then be deprotected using mild TFA conditions that would leave the *tert*-butyl protected carboxylic acids and the Boc-protected amine protection groups intact. After purifying the peptide with all amines and side chain carboxylic acids protected and a free carboxylic acid C-terminus, the rest of the steps would be identical to our current method as *tert*-butyl and Boc protection groups can both be deprotected with 95% TFA.

1.2.3 Deprotection of Boc-melittin-$CONH_2$

The next day, the film containing Boc-melittin-$CONH_2$ was dissolved in 1 mL of an ice-cold solution of 95:5 TFA:DMF and stirred at room temperature for one hour to deprotect the N-terminal amine and lysine side chains. The solution was diluted with 15 mL H_2O and 4 mL acetontrile before being HPLC purified using a gradient of 20-95%. Native melittin (melittin-$CONH_2$) and melittin-COOH co-elute from the HPLC column. The fraction containing these species was collected and lyophilized.

1.2.3 Separation of amidated melittin from melittin-COOH

Lyophilized melittin and melittin-COOH were dissolved in 4 mL of a buffer containing 50 mM HEPES, pH 7.2, 200-mM NaCl and loaded onto a 5 mL HiTrap SP HP (Cytiva, Marlborough, MA) cation exchange chromatography column at a flow rate of 1.5 mL/min. In addition to separating melittin-COOH from amidated melittin, cation exchange chromatography removes the TFA salts leftover from HPLC purification as confirmed by ^{19}F solution NMR measurements that did not detect any residual TFA in our triply labeled melittin, which set an upper limit of 10 μM TFA based on the signal-to-noise of our calibration experiments with samples spiked with TFA and the number of scans alotted to the ^{19}F NMR experiments. NMR samples that are doped with synthetic, unlabeled melittin do contain up to ~5 mM TFA, as the synthetic melittin is lyophilized as a TFA salt. We do not see any chemical shift changes in HSQC or TROSY resonances when samples are supplemented with TFA, indicating that at these concentrations, TFA does not perturb the structure of tetrameric melittin or monomeric denatured melittin for that matter. The column was washed with two column volumes of the intial buffer before a gradient of 200-mM to 2-M NaCl over 18 column volumes was used to elute melittin-COOH and melittin. The elution peak corresponding to melittin was then dialyzed against milli-Q water as a desalting step, using a 2 kDa cut-off Slide-A-Lyzer Dialysis Casette (Thermo Fisher Scientific, Waltham, MA) prior to being lyophilized.

2. NMR Sample Preparation and Spectroscopy

2.1 NMR Sample Preparation

2.1.1 Assignment sample

The uniformly ^{13}C,^{15}N-labeled perdeuterated sample used for chemical shift assignment was produced by dissolving lyophilized ^{2}H,^{13}C,^{15}N-labeled melittin in 220 μl of buffer containing 25-mM postassium phospate pH 7.0, 50 mM NaCl, 3% D_2O. The final peptide concentration was 1.0 mM, as determined by the solution's absorbance at 280 nm (A_{280}) (Nanodrop 2000, Thermo Fisher Scientific, Waltham, MA). The solution was then loaded into a 5-mm outer diamater, 2.8-mm inner diameter, zirconia pressure cell rated for up to 3 kbar of hydrostatic pressure (Daedalus Innovations, Aston, PA).[11]

2.1.2 Isotropic sample for J-coupling measurements

The sample used for isotropic J-coupling measurements was produced by dissolving 375-μM ^{2}H,^{13}C,^{15}N-labeled melittin and 625-μM unlabeled synthetic melittin (synthesized by Dr. Galina Abdoulaeva, FDA Center for Biologics Evaluation & Research) in 180 μl of buffer containing 25-mM postassium phospate pH 7.0, 50-mM NaCl, 250-μM benzamidine, and 3% D_2O. The benzamidine was added to block proteolysis from trace amounts of proteases in the samples.[12] The sample was then loaded into a 3-mm outer diameter NMR sample tube.

2.1.3 Pf1 liquid crystal aligned sample for RDC measurements

The Pf1 liquid crystal aligned sample used to measure anistropic J+D-couplings was produced by dissolving 910 μM ^{2}H,^{13}C,^{15}N-labeled melittin into buffer containing 11 mg/ml Pf1 filamentous phage[13] (ASLA biotech, Riga, Latvia) 25 mM potassium phosphate pH 7.0, 700 mM NaCl, 250 μM benzamidine, and 5% D_2O. The Pf1 filamentous phage was purchased from ASLA biotech as a 50 mg/ml stock solution in 10-mM potassium phosphate pH 7.6, 2-mM $MgCl_2$, and 0.05% NaN_3. 180 μl of solution was then loaded into a 3-mm outer diameter NMR sample tube. Pf1 has a negative surface charge, while melittin is positively charged. At NaCl concentrations below ~400 mM, melittin and Pf1 have such strong electrostatic interactions that they crash out of solution. Higher concentrations of NaCl disrupt these electrostatic interactions and allow melittin signals to be observed by solution state NMR. Additionally, the high salt concentrations push the equilibrium towards the tetrameric state, which facilitates RDC measurements of tetrameric melittin.

We note that we also attempted to align melittin in other liquid crystal media, but were unable to find conditions suitable for RDC measurements of tetrameric melittin. Melittin was overaligned in both pentaethylene glycol monododecyl ether:hexanol (C12E5:hexanol) and pentaethylene glycol monooctyl ether:octanol (C8E5:octanol) liquid crystal samples[14]; the backbone ^{15}N-^{1}H resonances were broadened out below detection and only broad glutamine side chain -NH_2 peaks were observed in HSQC spectra across the entire temperature range tested. To test whether introducing positive charges to the liquid crystal would limit the interactions between positively charged melittin and the liquid crystal media, we doped the C12E5:hexanol and C8E5:octanol liquid crystals with cetrimonium bromide (CTAB), but melittin remained overaligned and its backbone resonances were not detectable in HSQC spectra. Squalamine was an attractive liquid crystal media because it is positively charged, which we expected to limit the attractive forces between melittin and the media.[15] Unfortunately, squalamine is insoluble in phosphate buffer, insoluble at high pH, and does not form a liquid crystalline phase in high ionic strength buffers, all of which are conditions that drive the melittin equilibrium towards the tetrameric state. We were therefore unable to find conditions in which squalamine formed a liquid crystalline phase and melittin is predominantly in a helical, tetrameric conformation.

2.1.4 Stretched polyacrylamide aligned sample for RDC measurements

340 μl cylindrical polyacrylamide gels were cast in 5.4 mm inner diameter tubes. The polyacrylamide gels consisted of 6.3% w/v acrylamide, 0.18% w/v N,N'-methylbisacrylamide, 0.51% w/v positively charged (3-acrylamidopropyl)-trimethylammonium chloride (ATAC), 0.2% w/v N,N,N',N'-tetramethylethylenediamine (TEMED), and 0.1% w/v ammonium persulfate (APS) in 150 mM Tris buffer, pH 8.0. Stock solutions of 40% w/v acrylamide, 2% w/v N,N'-methylbisacrylamide, and 75% w/v ATAC were thoroughly mixed in the Tris buffer to obtain the desired concentrations of each component. 0.2% w/v TEMED was then added to the solution and thoroughly mixed in before the addition of a freshly prepared 10% w/v stock solution of APS to a final concentration of 0.1% w/v. The solution was then dispensed into the 5.4 mm tubes and topped with 1-butanol to limit access to atmospheric O_2 and allowed to set at room temperature for one hour.

After the gels had fully set, they were transferred to 50 ml of 50 mM sodium phosphate buffer, pH 7.0 to dialyze for 16 hours. The gels were then dialyzed against 50 ml of milliQ water for 2.5 days, while exchanging the milliQ water each morning and evening. At this point, the gels had swelled to considerably larger volumes than they were initially cast due to the osmotic pressure. The gels were then dried at room

temperature for three days on weigh boats. They were periodically rotated to ensure even drying and to avoid letting the gels stick to the weigh boat surface.

The dried gel was then swelled with 440 µl of 200 µM ^{2}H,^{13}C,^{15}N-labeled melittin and 3.8 mM natural abundance synthetic melittin in 20 mM sodium phosphate buffer pH 7.0, 500 µM benzamidine, and 5% D_2O for 36 hours such that the final polyacrylamide concentration was 5% w/v and the gel had swelled to a diameter of 5.9 mm. The gel was then radially compressed and axially stretched into a 5.0 mm outer diameter (4.2 mm inner diameter) open ended NMR tube by means of a funnel with an airtight piston attached on one side.[16]

A comparitively high peptide concentration (4.0 mM vs. 0.91 mM used for measuring RDCs in the sample aligned with Pf1) was used in the stretched polyacrylamide gel sample to push the equilibrium towards the tetrameric state even in a relatively low ionic strength buffer (20 mM phosphate vs. 25 mM phosphate, 700 mM NaCl for the Pf1 sample).

2.2 NMR Spectroscopy

2.2.1 HNCA and HNCO experiments for backbone resonance assignment

3D TROSY-HNCA[17] experiments were run on an 800-MHz Bruker Avance-II spectrometer equipped with a 5-mm triple axis gradient cryoprobe. Data was acquired using a 10.4% non-uniform sampling schedule when the sample was at atmospheric pressure for a total experimental time of 37 hours and a 12.1% sampling schedule for a total experimental time of 43.1 hours when the sample was pressure-denatured with 2.25 kbar of hydrostatic pressure. Four scans were collected per transient with 106.5 ms of ^{1}H acquisition time. The ^{15}N indirect dimension was acquired with a 27.41 ppm sweepwidth and 67.5 ms of evolution, while the ^{13}C indirect dimension was acquired with a 27.92 ppm sweepwidth and 35.1 ms of evolution. These experiments employed standard $1/(2J_{average})$ = 5.4 ms ^{1}H-^{15}N and ^{15}N-^{1}H INEPT transfer steps and a 20 ms ^{15}N-$^{13}C\alpha$ transfer step.

3D TROSY-HNCO experiments[17] were run on a 600-MHz Bruker Avance Neo spectrometer equipped with a 5-mm cryoprobe with a z-axis gradient. Data was acquired using a 16.0% non-uniform sampling schedule for a total experimental time of 20.9 hours when the sample was at atmospheric pressure and a 16.5% sampling schedule for a total experimental time of 21.5 hours when the sample was pressure-denatured with 2.25 kbar of hydrostatic pressure. A total of 4 scans were collected per transient with 106.5 ms of ^{1}H acquisition time. The ^{15}N indirect dimension was acquired with a 28.35 ppm sweepwidth and 87.0 ms of evolution, while the ^{13}C indirect dimension was acquired with an 11.00 ppm sweepwidth and 42.2 ms of evolution. These experiments employed standard $1/(2J_{average})$ = 5.4 ms ^{1}H-^{15}N and ^{15}N-^{1}H INEPT transfer steps and a 24 ms ^{15}N-$^{13}C'$ transfer step.

Chemical shift assignment of the pressure denatured state was done by increasing the hydrostatic pressure of the sample cell to 2.25 kbar using a home built in situ NMR pressure jump apparatus.[18] This apparatus is typically used for pressure jump experiments, but can also be utilized for static high pressure experiments. The HNCA and HNCO experiments were collected at 15 °C and utilized a mixed-time evolution scheme in the indirect dimensions to extend acquisition times past what a constant-time experiment allows.[19] Chemical shifts are shown in tabular form in **Table S2**.

2.2.2 ARTSY experiments for measuring $^{1}D_{NH}$ RDCs

Values of the NH anisotropic J+D couplings in the aligned samples and the J couplings in the isotropic sample were measured with an ARTSY experiment[19] where the initial ^{1}H-^{15}N INEPT is set to 10.75 ms (~$1/^{1}J_{NH}$). Th reference spectrum consists of 5.38 ms of ^{15}N-^{1}H dephasing by placing the ^{15}N 180° halfway between the first ^{1}H 180° and the second ^{1}H 90°, while the attenuated spectrum corresponds to having the ^{15}N 180° pulse directly after the first ^{1}H 180° for a total dephasing time of 10.75 ms. Isotropic J-couplings were measured at 15 °C on a 700-MHz spectrometer equipped with a triple-axis gradient cryoprobe, whereas anisotropic J+D couplings were measured at 20 °C on an 800-MHz spectrometer equipped with a triple-axis gradient cryoprobe. Isotropic, Anistropic, and $^{1}D_{NH}$ couplings can be found in tabular form in **Table S3**. ARTSY experiments were signal averaged for 23.4 hours for the isotropic sample, 31.9 hours for Pf1, and 68.5 hours for the the stretched polyacrylamide gel sample.

3. Data Processing, Structural Model Development, and Analysis

3.1 NMR Data processing

3.1.1 Reconstruction and processing of the assignment HNCA and HNCO spectra

The non-uniform sampled TROSY-HNCA and TROSY-HNCO experiments were reconstructed with SMILE[21] and processed with NMRpipe.[22] The ARTSY experiments were fully sampled and collected in an interleaved fashion. The data was split with the COADD function prior to being processed in NMRPipe.

3.2 AlphaFold-Multimer Implementation

The AlphaFold2[23] source code including the AlphaFold-Multimer[24] (AF-M) plugin for predicting structures of homooligomeric proteins was retrieved from the GitHub repository (https://github.com/jcheongs/alphafold-multimer). Our implementation of AlphaFold-Multimer limits the sequences of input structures so that it excludes all of the initial input structures with greater than 30% sequence identity.[25–28]

AlphaFold2 limits the input to only include canonical amino acids; it does not provide a way to introduce unnatural amino acids or post-translational modifications. We hypothesized that the negative charge on the C-terminus of melittin-COOH impacts the tetrameric structure and that by neutralizing the negative charge of the C-terminal carboxylic acid with a positively charged sidechain, such as lysine (K) or arginine (R), we would be able to recover the native oligomeric structure of melittin in AF-M structure predictions.

To test whether this hypothesis was correct we generated five individual AF-M structural models for five separate mutants, totalling 25 AF-M structural models. We generated five structures for melittin-COOH (referred to as AF1-AF5), melittin-K-COOH (AFK1-AFK5), melittin-R-COOH (AFR1-AFR5), melittin-G-COOH (AFG1-AFG5), and melittin-D-COOH (AFD1-AFD5). AFK1-AFK5 and AFR1-AFR5 were meant to test our hypothesis directly, AF1-AF5 and AFG1-AFG5 were meant to be controls as we had no reason to believe they would recapitulate the true structure of tetrameric melittin, and AFD1-AFD5 as a negative control for our hypothesis, as our hypothesis would suggest an acidic sidechain on the C-terminus would perturb the structure significantly. Atomic coordinates for the AlphaFold-Multimer structural models can be downloaded from https://doi.org/10.5281/zenodo.7574383 (**Table S7**).

3.3 Data Analysis

3.3.1 Resonance assignment

Backbone ^{1}H, ^{15}N, and $^{13}C^{\alpha}$ resonance assignment of the sample at atmospheric pressure (1 bar) and pressure denatured (2.25 kbar) was done using a traditional backbone walk through the TROSY-HNCA spectra, while carbonyl shifts were determined from the TROSY-HNCO spectra. Peak picking and resonance assignment was done with NMRFAM-SPARKY.[29] Pressure-dependent corrections[30,31] were applied to chemical shifts measured at high pressure so that they were on equal footing and could be directly compared to chemical shifts obtained at atmospheric pressure. Deuterium isotope shift corrections were applied[32] so that the reported chemical shifts correspond to a protonated peptide, even though resonance assignment was done on a perdeuterated peptide. Chemical shifts assigned to the melittin tetramer at atmospheric pressure and the monomer under pressure denaturing conditions can be found in **Table S2**. These backbone chemical shifts were deposited in the Biological Magnetic Resonance Data Bank (BMRB) under entry 51703.

3.3.2 Extracting $^{1}D_{NH}$ couplings from experimental data

Isotropic J couplings and anisotropic J+D couplings were extracted as reported by Fitzkee & Bax.[19] Briefly, peak picking was done on the reference spectrum in NMRPipe such that the points above the full width at half max were included in the parabolic peak-picking interpolation. The intensity of the attenuated spectrum was then read off at the exact same position as was picked in the reference spectrum. The couplings are then calculated according to:

$$J\ (or\ J+D) = \frac{-1}{T} + \frac{2}{\pi T}\sin^{-1}\frac{Q}{2}$$

Where T is the length of the initial INEPT period (10.75 ms), and Q is the intensity ratio between the attenuated and reference spectrum. The error was calculated according to:

$$\sigma \approx \frac{1}{\pi T(S/N)}$$

where *S/N* refer to the signal-to-noise ratio in the reference spectrum. $^{1}D_{NH}$ values were then calculated by subtracting the isotropic J couplings from the anisotropic $J + D$ couplings, while their errors were added in quadrature. Measured couplings are reported in **Table S3**. The RDCs were deposited in the BMRB under entry 51703.

3.3.3 Comparison of $^{1}D_{NH}$ couplings with the crystal structure and AlphaFold-Multimer models

Protons were added to the 2MLT[33–35] X-ray crystal structure using DYNAMO.[22] To add in the protons, DYNAMO first creates an extended structure that includes protons. A simulated annealing step then folds this extended structure so that the heavy atom coordinates are as close as possible to the coordinates of the input structure. Then the heavy atoms and the hydrogen atoms that are bonded to them are moved to exactly match the heavy atom coordinates in the input structure. The asymmetric dimer that is deposited in the PDB was then symmetry expanded using PyMOL[36] to produce a tetrameric structure. The atomic coordinates of the 2MLT tetrameric structure with protons can be downloaded from https://doi.org/10.5281/zenodo.7574383 (**Table S7**). Residues for each monomer were given unique residue numbers (1-26…101-126…201-226…301-326). Residues in the AlphaFold-Multimer tetramer .pdb file were also renumbered using the same numbering scheme. Only one set of resonances was assigned to the folded tetrameric state; we did not see direct evidence for the slight asymmetry observed by Terwilliger & Eisenberg.[34] If there are two separate monomer conformations, their signals are averaged faster than the timescale of our NMR experiments. We therefore used the same $^{1}D_{NH}$ couplings for each of the four monomers when fitting the experimental RDC data to the structures. We used singular value

decomposition (SVD)[37] of the Saupe matrix[38] to determine the best fit parameters for the Saupe matrix and then to provide predicted $^1D_{NH}$ values based on the fitted alignment tensor. The SVD fitting routine weights each coupling by the inverse of its uncertainty so that precise RDCs with low uncertainity are more signficant in the fitting than RDCs with high uncertainty. Reported Q factors[39,40] are calculated according to:

$$Q = \frac{rms\left(\langle D_{exp}\rangle - D_{pred}\right)}{\sqrt{D_a^2(4+3Rh^2)/5}}$$

with separate sets of D_{pred} used for each of the four monomers in the tetramer. D_a is the magnitude of the dipolar coupling tensor, while Rh is the rhombicity. In addition to the crystallographic C_2 symmetry axis of the 2MLT X-ray crystal structure, there is a noncrystallographic two-fold symmetry axis where the two sets of monomers have similar structures, but do not overlay exactly and result in two distinct sets of bond vectors with respect to the alignment tensor. The AF-M structure has two approximate C_2 symmetry axes, though none of the monomers overlay exactly. We note that in an oligomeric species with symmetry axes, a principal component of the alignment tensor inherently lies along the symmetry axis.[41] Therefore, there are essentially only two free parameters, D_a and Rh, to be determined during the SVD fitting.[42] The normalized scalar product between the five element Saupe vectors corresponding to the alignment tensors of melittin in Pf1 and melittin in the stretched polyacrylamide gel was ~0.98 for the structures considered in this study, demonstrating that the alignment of melittin in in Pf1 and stretched polyacrylamide gels is essentially colinear. This is not surprising, considering the two C_2 symmetry axes in melittin already define the orientation of the alignment tensor. The only parameters that can vary in the weak alignment of melittin are the *Da*, which simply acts as a scaling factor for the RDCs, and the rhombicity.

SVD fitting results for the 2MLT crystal structure and the 25 AF-M structural models including the Q factor, *Da* (Hz), *Rh*, and the *RMS* between the experimental and predicted couplings for $^1D_{NH}$ RDCs measured in Pf1 alignment media and the positively charged polyacrylamide gel alignment media are tabulated in **SI Table 4** and **SI Table 5**, respectively. Residue Q26 was excluded from all fits due to its dynamic disorder. The predicted RDCs for residues R24 and Q25 in the majority of the AF-M structural models do not fit the experimental data (**Fig. S7j-l, S8j-l**) and including them in the fit results in a poor fit to the experimental data and subsequently a larger Q factor. Excluding residues R24 and Q25 from the 2MLT fit results in the same Q factor as including them. The experimental data fits many of the AF-M structures for residues G3-K23 better, while residues R24 and Q25 fit better for the 2MLT X-ray crystal structure. The poor fit for the C-terminal residues in the AF-M structure appears due to the non-native C-termini, disrupting the hydrogen bonding pattern observed in the final helical turn of the native melittin crystal structure.

Care must be taken when analyzing, interpreting, and comparing our $^1D_{NH}$ couplings because hydrogens were incorporated into the x-ray crystal and the AlphaFold-Multimer structures in different ways. Using DYNAMO to add hydrogens to crystal structures, as we have done for the 2MLT structure, has been shown to be very robust and reliable.[25,43] Hydrogens are not included during the AF-M neural network structure prediction process; they are added during a final Amber relaxation step.[44,45] To test whether the better Q factor we observed for the AF-M structural models is influenced by the Amber relaxation step, we added protons to the unrelaxed model utilizing the same procedure used for the 2MLT crystal structure. SVD fitting of $^1D_{NH}$ couplings for residues G3-K23 resulted in Q factors within 5% of the Q factors for the relaxed model. Therefore, the amber relaxation step neither improved nor worsened the agreement between experimental RDCs and the AF-M structural model.

The AF-M model confidence scores is a metric that combines the interface predicted template modeling score (ipTM) and the predicted template modeling score (pTM) in an 8:2 ratio to give an overall

predicted template modeling score. The ipTM measures the predicted quality of the oligomeric assembly, while the pTM predicts the quality of the monomeric units within the oligomer. TM-scores are a measure of how close a structural model is expected to be to the true structure, where a value of one is an identical structure. TM-scores above 0.5 are considered to have the same general fold and three dimensional structure.[46] We therefore chose to consider AF-M models with confidence scores above 0.5 to be good models and AF-M models with confidence scores below 0.5 to be poor models. All of the models with confidence scores above 0.5 had Q factors ranging from 0.14 to 0.25, which would be considered medium to high quality by most NMR spectroscopists (**Fig. S9a,b**). A number of models yielded poor AF-M model confidence scores, with two of these nevertheless showing excellent Q factors (models AF3 and AFR4 in **Tables S4, S5, and S6**). These models differ strongly from the 2MLT structure (backbone coordinate RMSDs > 8 Å relative to 2MLT) but showed low Q factors, which appeared to be artifacts of large $|D_a|$ values that increase the denominator used in Q factor calculations (see legend to **Fig. 3**, main text).[47]

The fact that the AF-M model confidence scores accurately determine whether a structural model will be within ~2.0 Å of the true structure (confidence score > 0.5) or greater than 4.0 Å from the true structure (confidence score < 0.5) for tetrameric melittin confirms that this scoring system will be an excellent tool for screening out inaccurate oligomeric protein structures. Although two (AFR1 and AFK1) out of the top three (AFR1, AFK1, and AFG3) AF-M structural models in our fits to the RDC data had a positively charged C-terminal extension, suggesting that our initial hypotheses about what C-terminal extensions would promote a tetrameric structure most similar to melittin in solution may be correct, there was not a clear trend between our initial hypotheses and the overall distribution of Q factors in the 25 AF-M structural models. It will be interesting to see experimentally which, if any, of these mutants form a stable tetramer in solution and to validate their structures with RDCs. Unfortunately, the AF-M confidence score alone only reveals whether an AF-M structural model is in the right ball park. This is exactly where combining AF-M model confidence scores with a technique that is exquisitely sensitive to small structural differences, such as RDC measurements, holds promise to greatly accelerate high-resolution structure determination of oligomeric systems in solution.

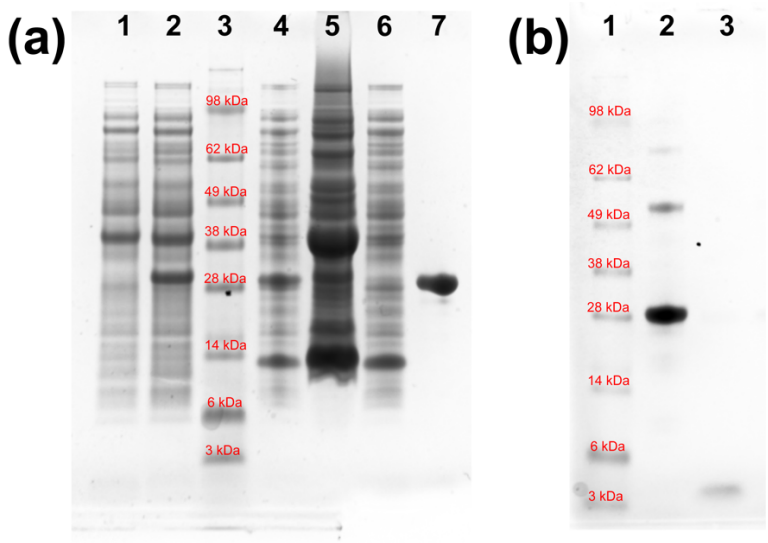

Figure S1. $^{2}H,^{13}C,^{15}N$-labeled Melittin-COOH expression and purification SDS-PAGE gels.
(a) Expression and purification of GST-TEV-mel-COOH.

1) Expression culture right before induction
2) Expression culture at harvest.
3) Ladder
4) Soluble fraction of lysate
5) Insoluble fraction of lysate
6) GST affinity column flow through
7) GST affinity column elution

(b) Separation of GST and TEV from melittin-COOH.

1) Ladder
2) TEV protease + residual GST
3) melittin-COOH

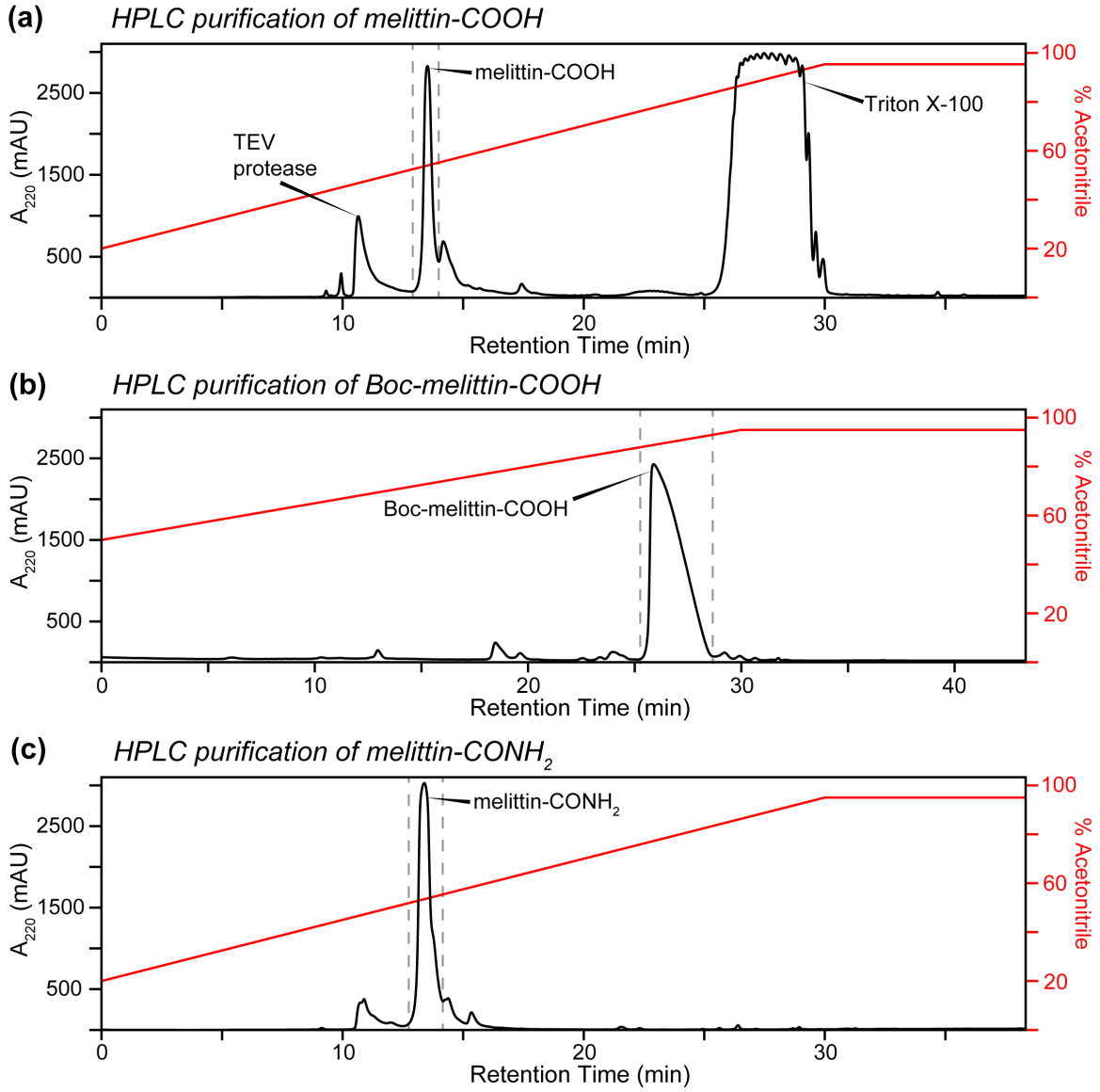

Figure S2. Reverse phase HPLC chromatograms. All HPLC purifications were done with 0.05% TFA as the ion pairing agent with a Phenomenex Jupiter 4-μm Proteo 90-Å 250 × 10.00 mm column. (a) Purification of melittin-COOH. After loading the sample and washing the column with 20% acetonitrile, the sample was eluted using a 20%-95% acetonitrile gradient over 30 minutes, followed by a 95% acetonitrile wash for 8.3 minutes. This step is done to separate melittin-COOH from TEV, Triton X-100 and residual GST. It also acts as a desalting step, which is needed for the subsequent organic reactions. (b) Purification of Boc-melittin-COOH. After loading the sample and washing the column with 50% acetonitrile, Boc-melittin-COOH was eluted with a 50-95% acetonitrile gradient over 30 minutes, followed by a 13.3-minute wash with 95% acetonitrile. (c) Purification of native melittin (melittin-$CONH_2$). After loading the sample and washing the column with 20% acetonitrile, native melittin was eluted with a 20-95% acetonitrile gradient over 30 minutes, followed by a 95%-acetonitrile wash for 8.3 minutes. The gray dashed lines denote which part of the eluent was collected and lyophilized for subsequent steps.

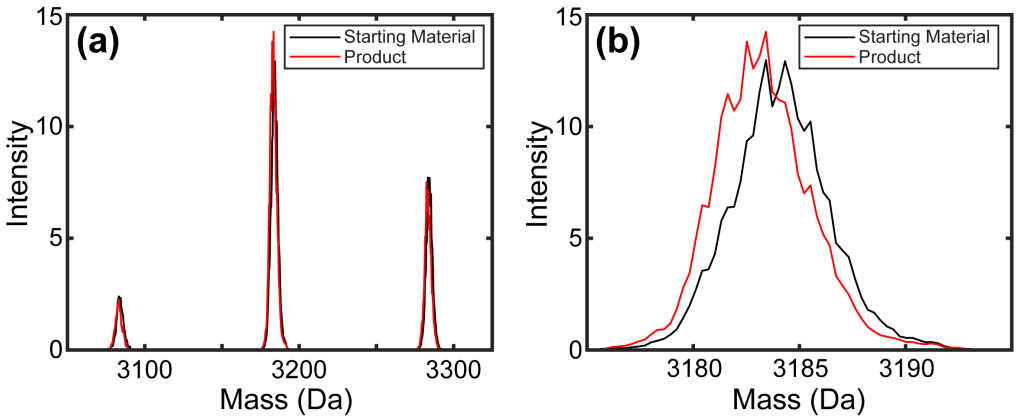

Figure S3. Liquid chromatography mass spectrometry (LCMS) of the amidation reaction on ^{15}N-labeled Boc-melittin-COOH with $^{14}NH_4Cl$. (a) Full mass range. (b) Zoomed in region corresponding to the central peak in (a). The starting material is ^{15}N-labeled Boc-melittin-COOH, while the the product is Boc-melittin-$CO^{14}NH_2$. Note that amidation with $^{15}NH_4Cl$ results in indistinguishable masses for the product and starting material. However, when amidation is performed with $^{14}NH_4Cl$, the mass decreases by 1.0 Da, which is easily observed in the mass spectra. We observed multiple products from the Boc-protection reaction, corresponding to incomplete Boc-protection of all amines. However, we saw no evidence of intramolecular lactams in our final products. Therefore, the sites that are unreactive to Boc_2O are also less reactive during the HATU coupling reaction.

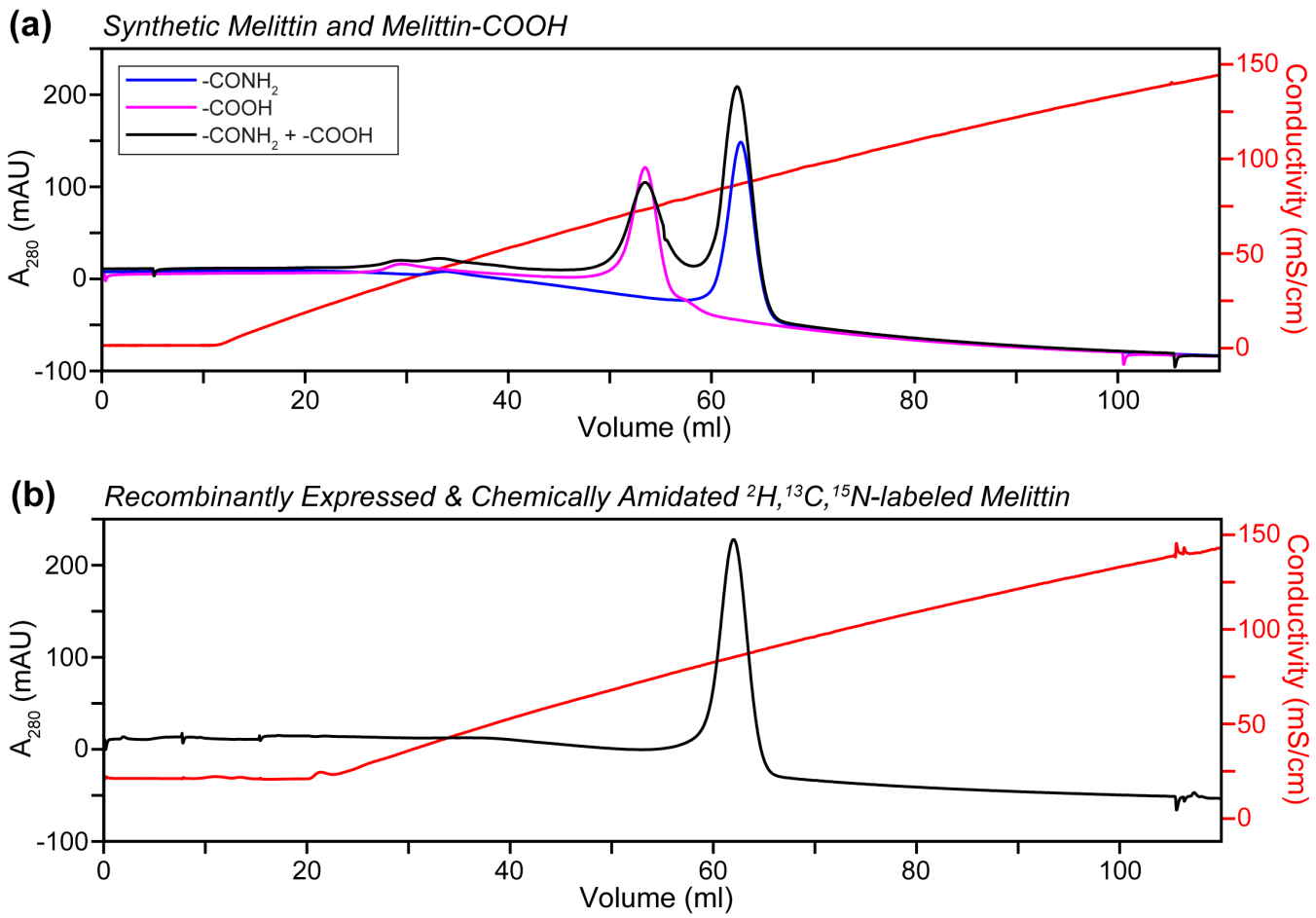

Figure S4. Ion exchange chromatography to separate melittin from unreacted melittin-COOH. (a) Overlaid chromatograms where synthetic melittin (melittin-$CONH_2$), synthetic melittin-COOH, and a solution containing both synthetic melittin and synthetic melittin-COOH are purified via cation exchange chromatography. The loading and wash buffer were 50-mM HEPES; the sample was eluted with a 0-M to 2-M NaCl gradient over 20 column volumes. We were able to obtain reasonably good separation between the carboxylic acid and amidated peptide with ion exchange chromatography even though we were unable to separate these species with reverse phase HPLC. (b) Chromatogram of the ion exchange chromatography purification of recombinantly expressed and chemically amidated $^{2}H,^{13}C,^{15}N$-labeled melittin. The peptide was loaded in 50-mM HEPES pH 7.2, 200-mM NaCl buffer and the column was washed with the same buffer. Melittin was then eluted with a 200-mM to 2-M NaCl gradient over 18 column volumes. No detectable amount of unreacted melittin-COOH remained in this sample, demonstrating the the amidation reaction went to completion. However, in previous production runs we did observe up to 15% melittin-COOH from incomplete reactions and then chose to include this purification step to ensure the absence of detectable amounts of melittin-COOH and to remove residual TFA.

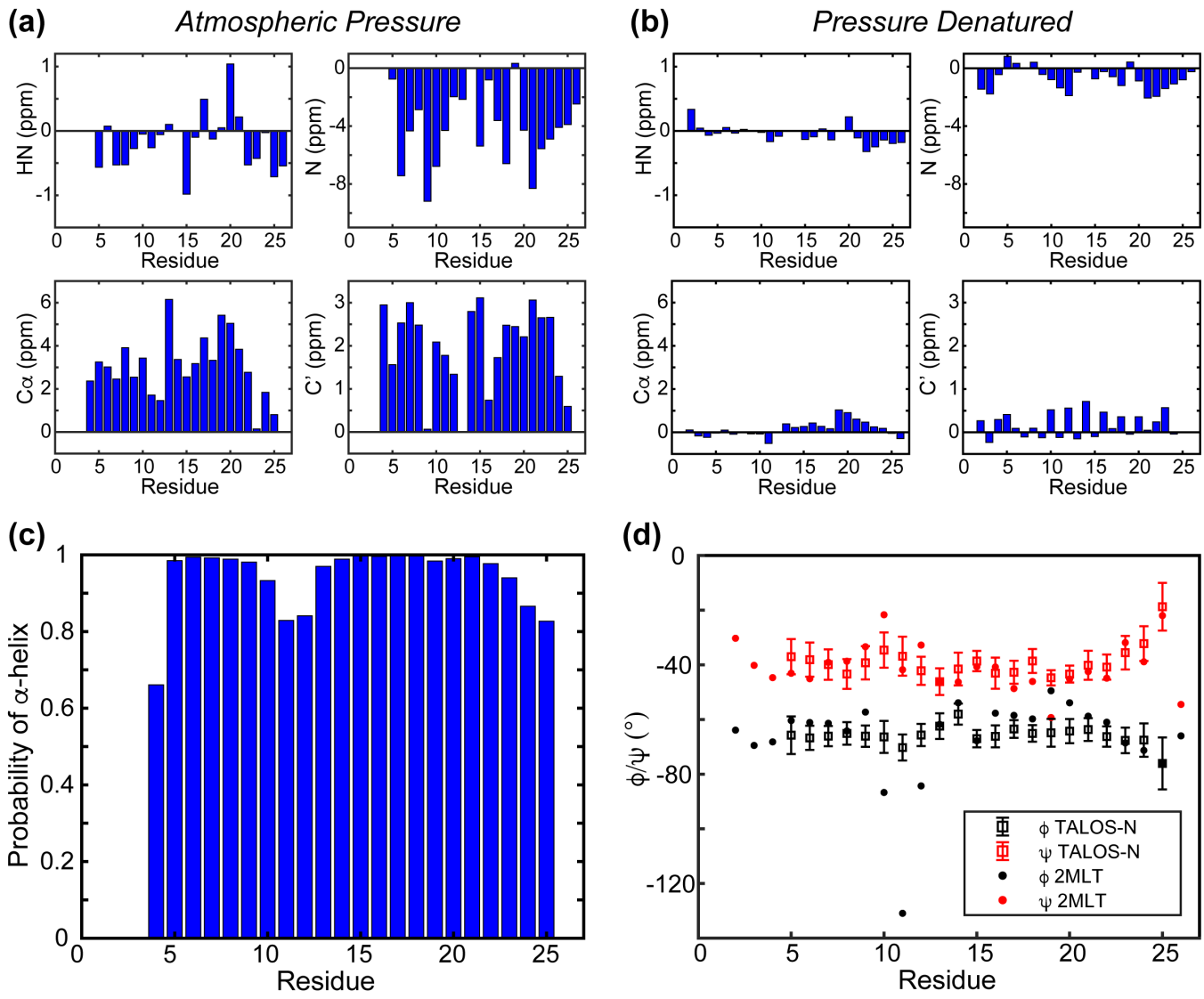

Figure S5. Secondary shifts and TALOS-N predicted secondary structure.[48] (a) Backbone secondary shifts for resonances assigned to the folded tetramer at atmospheric pressure. The ^{15}N, $^{13}C^{\alpha}$, and $^{13}C'$ secondary shifts are all indicative of α-helical secondary structure. (b) Backbone secondary shifts for pressure-denatured (2.25 kbar) melittin. These secondary shifts are close to the expected random coil values,[49] but show some evidence for transient α-helical structure. (c) Probability of α-helical secondary structure at 1 bar, determined by TALOS-N. Although TALOS-N predicts that the entire peptide is most likely α-helical, its confidence is lower for the residues that were observed to be in a kink in the 2MLT crystal structure. (d) (ϕ,ψ) backbone torsion angles predicted by TALOS-N, measured in the 2MLT X-ray crystal structure, and measured in the AlphaFold-Multimer structure. The 2MLT crystal structure consists of an asymmetric dimer and therefore has two sets of torsion angles for each residue, while the AlphaFold-Multimer structure consists of four sets of torsion angles because its structure prediction procedure does not strictly enforce symmetry. The two sets of torsion angles in the 2MLT structure are quite similar and overlap for most residues except for the termini and in the kink region. The four monomers in the AlphaFold-Multimer tetramer have essentially indistinguishable torsion angles for all residues.

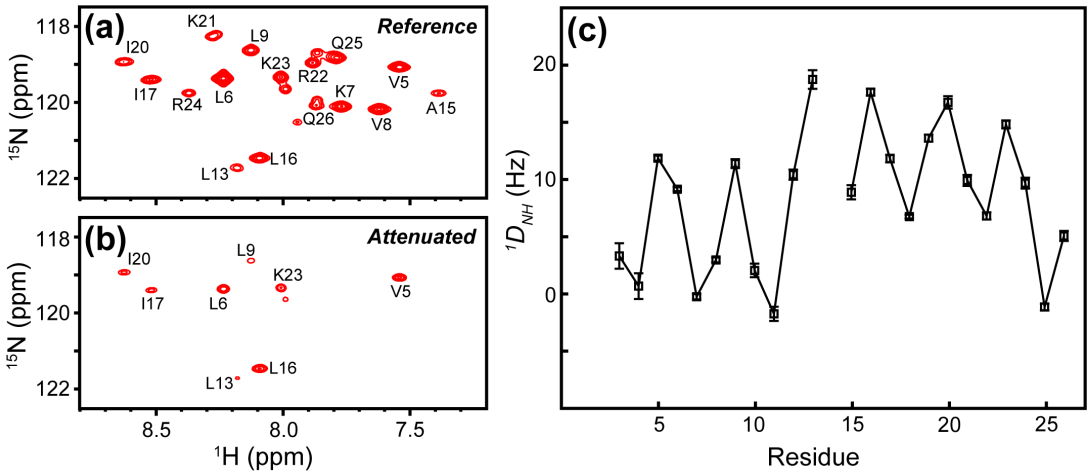

Figure S6. Representative ARTSY spectra of ^{2}H,^{13}C,^{15}N-labeled melittin aligned with 11 mg/ml Pf1 filamentous phage at 20 °C in an 18.8-T magnet and the correspond extracted $^{1}D_{NH}$ values. (a) Reference spectrum with an effective ^{1}H-^{15}N dephasing time of 5.375 ms. (b) Attenuated spectrum with an effective ^{1}H-^{15}N dephasing time of 10.75 ms. Intense positive peaks in the attenuated spectrum correspond to J+D couplings that are significantly greater than -93 Hz (corresponding to positive $^{1}D_{NH}$ values). (c) Extracted $^{1}D_{NH,Pf1}$ couplings.

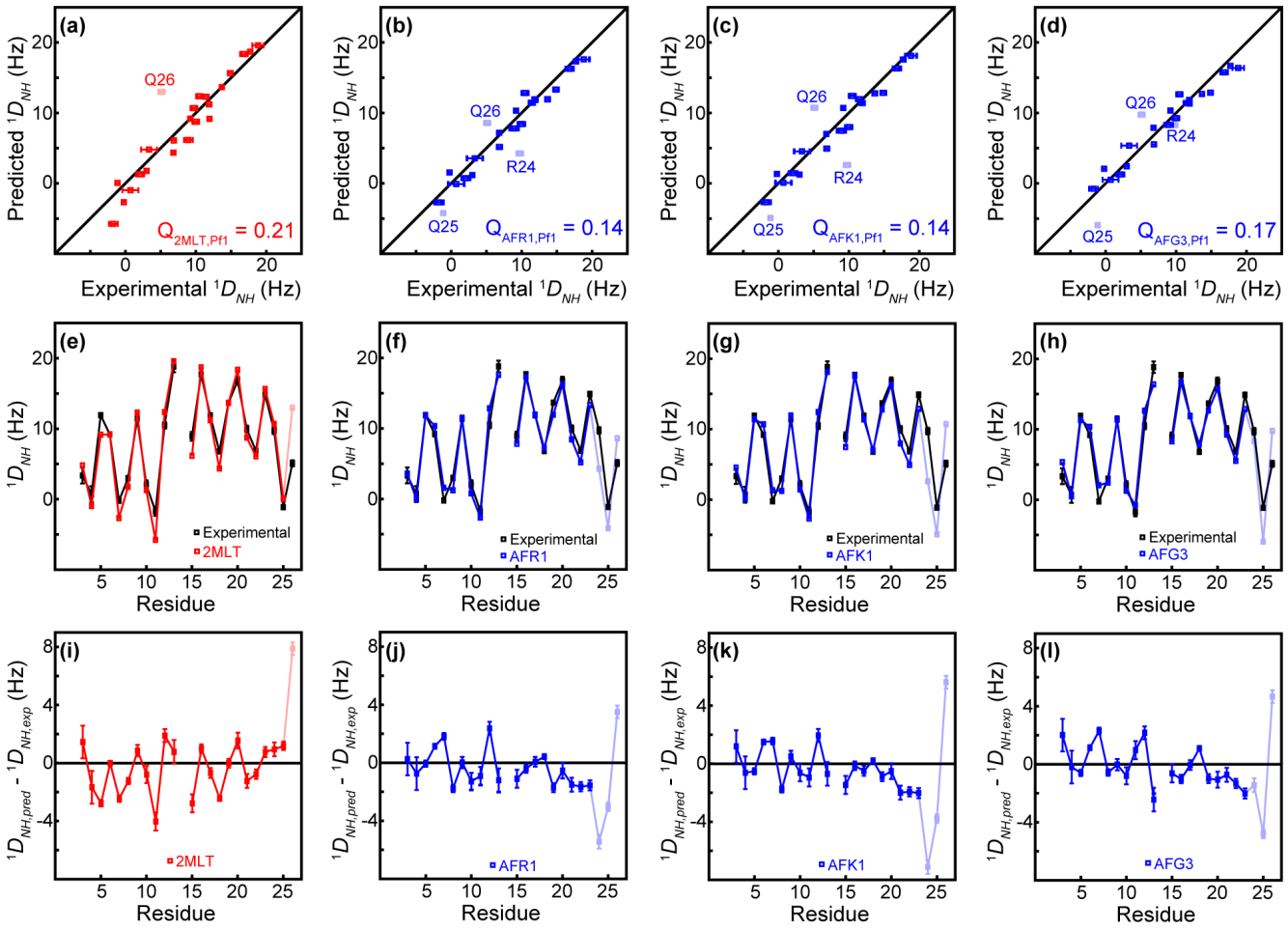

Figure S7. Experimental and predicted $^1D_{NH}$ values for the Pf1 aligned sample. (a-d) Predicted vs. experimental $^1D_{NH}$ correlation plots. (e-h) Residue-specific experimental and averaged predicted $^1D_{NH}$ RDCs. (i-l) Differences between the averaged predicted and experimental RDCs used in the SVD fit. (a,e,i) Plots for the 2MLT crystal structure. (b,f,j) Plots for the AFR1 (melittin-R-COOH with the AF-M model confidence score) structural model. (c,g,k) Plots for the AFK1 (melittin-K-COOH with the best AF-M model confidence score) structural model. (d,h,l) Plots for the AFG3 structural model (melittin-G-COOH with the third best AF-M model confidence score).

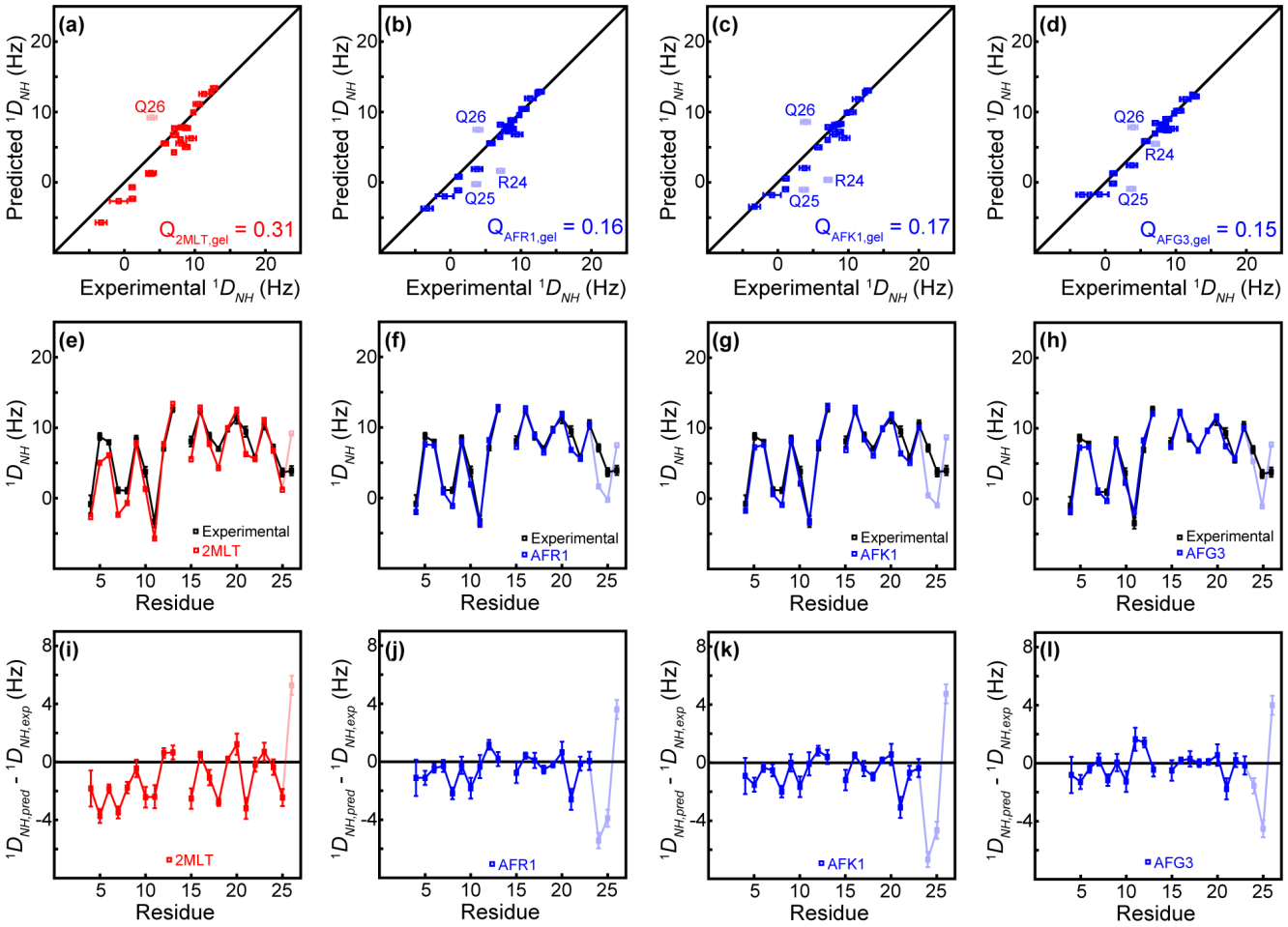

Figure S8. Experimental and predicted $^1D_{NH}$ values for the stretched polyacrylamide gel aligned sample. (a-d) Predicted vs. experimental $^1D_{NH}$ correlation plots. (e-h) Residue-specific experimental and averaged predicted $^1D_{NH}$ RDCs. (i-l) Differences between the averaged predicted and experimental RDCs used in the SVD fit. (a,e,i) Plots for the 2MLT crystal structure. (b,f,j) Plots for the AFR1 (melittin-R-COOH with the best AF-M model confidence score) structural model. (c,g,k) Plots for the AFK1 (melittin-K-COOH with the best AF-M model confidence score) structural model. (d,h,l) Plots for the AFG3 structural model (melittin-G-COOH with the third best AF-M model confidence score).

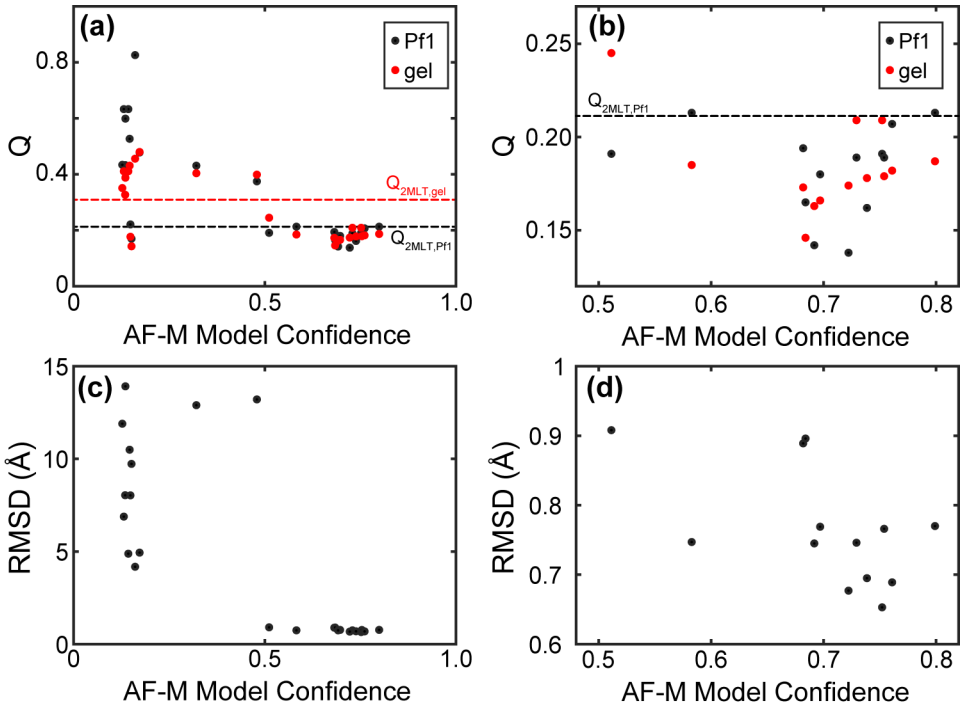

Figure S9. Relationship between the AlphaFold-Multimer confidence score and Q factors. (a) Correlation between AF-M confidence scores and RDC Q factors for the 25 AlphaFold-Multimer structures considered in this study. Dashed horizontal lines indicate the Q factors for the 2MLT crystal structure in the Pf1 sample (black) and the stretched polyacrylamide gel sample (red). (b) A zoomed in view from (a) shows that for model confidence scores above 0.5 there is no correlation between RDC Q factors and the AF-M confidence score. (c) Correlation between confidence scores and the backbone RMSD between each AlphaFold-Multimer model and the 2MLT crystal structure. All structural models with confidence scores above 0.5 were in excellent agreement with the crystal structure, while none of the models with confidence scores below 0.5 were in agreement with the 2.0 Å-resolution crystal structure. (d) Zoomed in view from (c) showing that there is not a particularly strong correlation between the AF-M confidence score and the backbone RMSD for these models, which is expected since the crystal structure was only solved to 2.0 Å resolution.

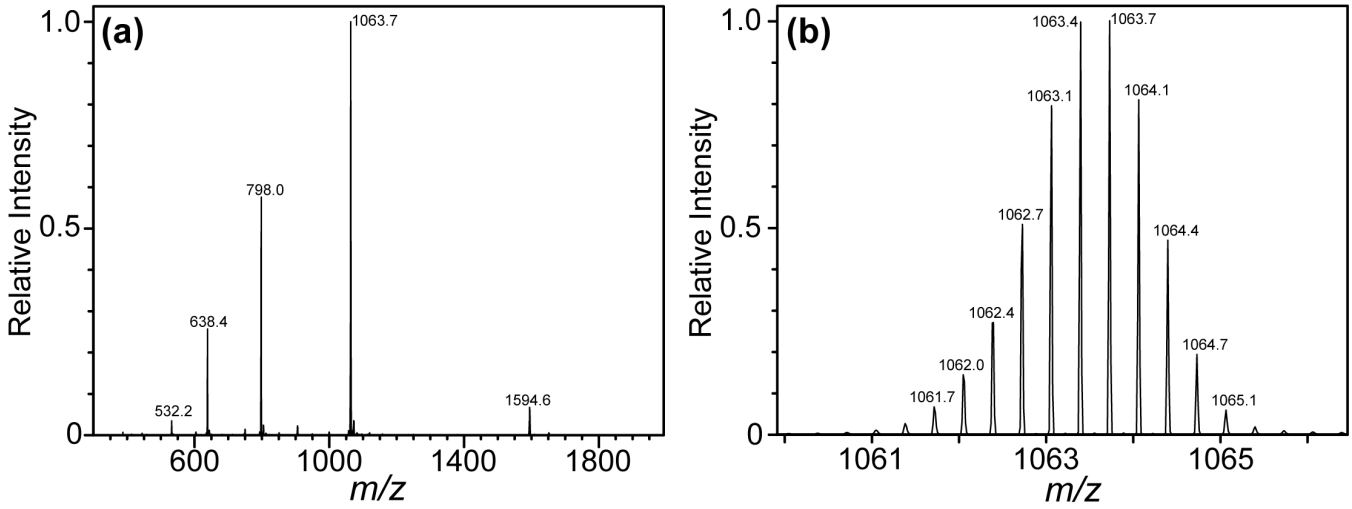

Figure S10. Positive electrospray ionization mass spectrometry of $^{2}H,^{13}C,^{15}N$-labeled melittin. (a) Full mass spectrum. (b) Zoomed in view of the +3 state, showing individual isotopologues. The theoretical *m/z* is 1065.0666 for the +3 charge state, assuming full $^{2}H,^{13}C,^{15}N$ incorporation and ^{1}H back exchange for the 50 exchangeable hydrogen atoms in melittin. The atomic makeup of fully $^{2}H,^{13}C,^{15}N$-labeled melittin is 50 natural abundance H nuclei, 31 natural abundance O nuclei, 131 ^{13}C nuclei, 179 ^{2}H nuclei, and 39 ^{15}N nuclei.

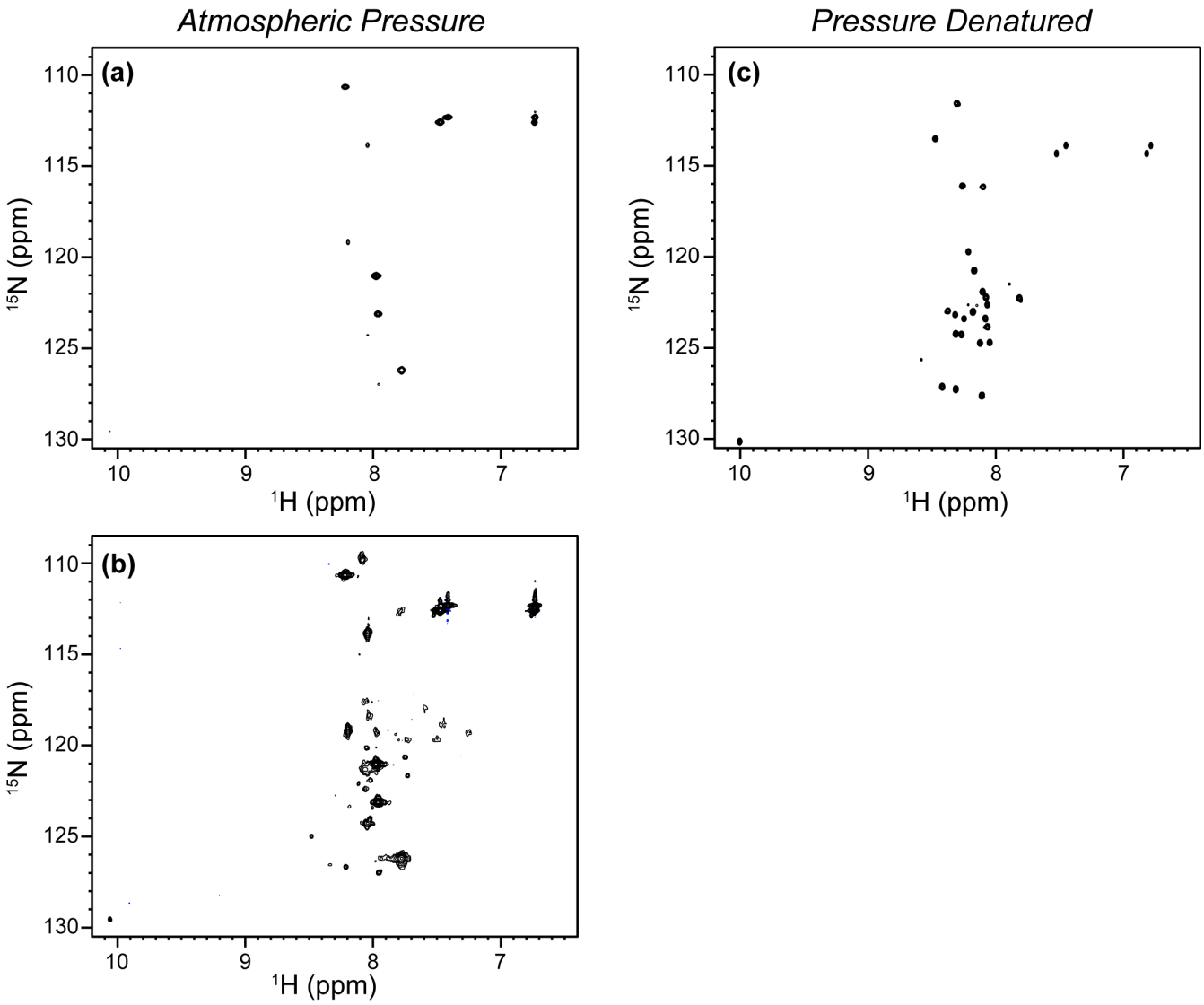

Figure S11. HSQC spectra of 1.0-mM melittin-COOH at 20 °C in 25-mM potassium phosphate buffer pH 7.0, 50-mM NaCl, and 3% D_2O on a 600-MHz spectrometer. (a) HSQC spectrum at atmospheric pressure. Note that only a handful of resonances are observed. (b) The same spectrum as depicted in (a) but plotted with significantly lower contour levels so that very weak and exchange-broadened peaks can be observed. (c) Pressure-denatured (2.4 kbar) spectrum of melittin-COOH. Each spectrum took 24 minutes to acquire.

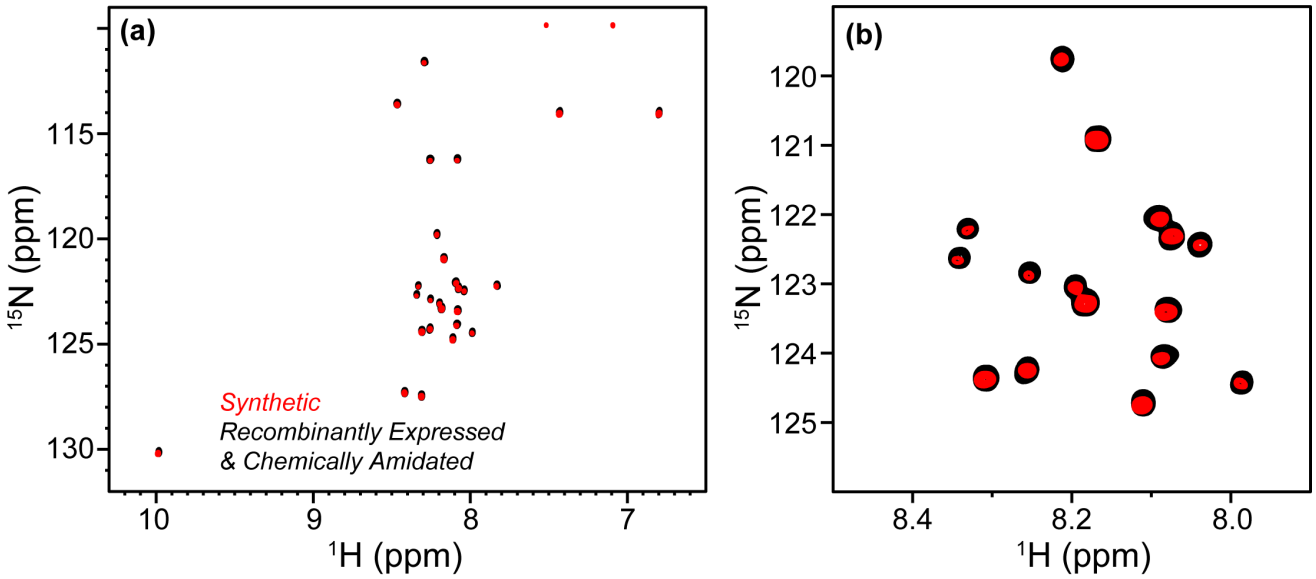

Figure S12. Pressure-denatured HSQC spectrum comparison of natural abundance synthetic melittin (red) and recombinantly expressed, chemically amidated ^{15}N-labeled melittin (black). These spectra were collected with 1.0-mM melittin in 25-mM potassium phosphate, 50-mM NaCl, 3% D_2O at 15 °C and 2.4 kbar on an 800-MHz spectrometer. The natural abundance HSQC spectrum was signal averaged for 11 hours to obtain suitable signal-to-noise, while the ^{15}N-labeled HSQC took 14 minutes. (a) Full view of the HSQC spectrum. (b) Zoomed in view of the most densely populated region of the HSQC spectrum. The chemical shifts for the two peptides are identical, showing that the two peptides are chemically identical.

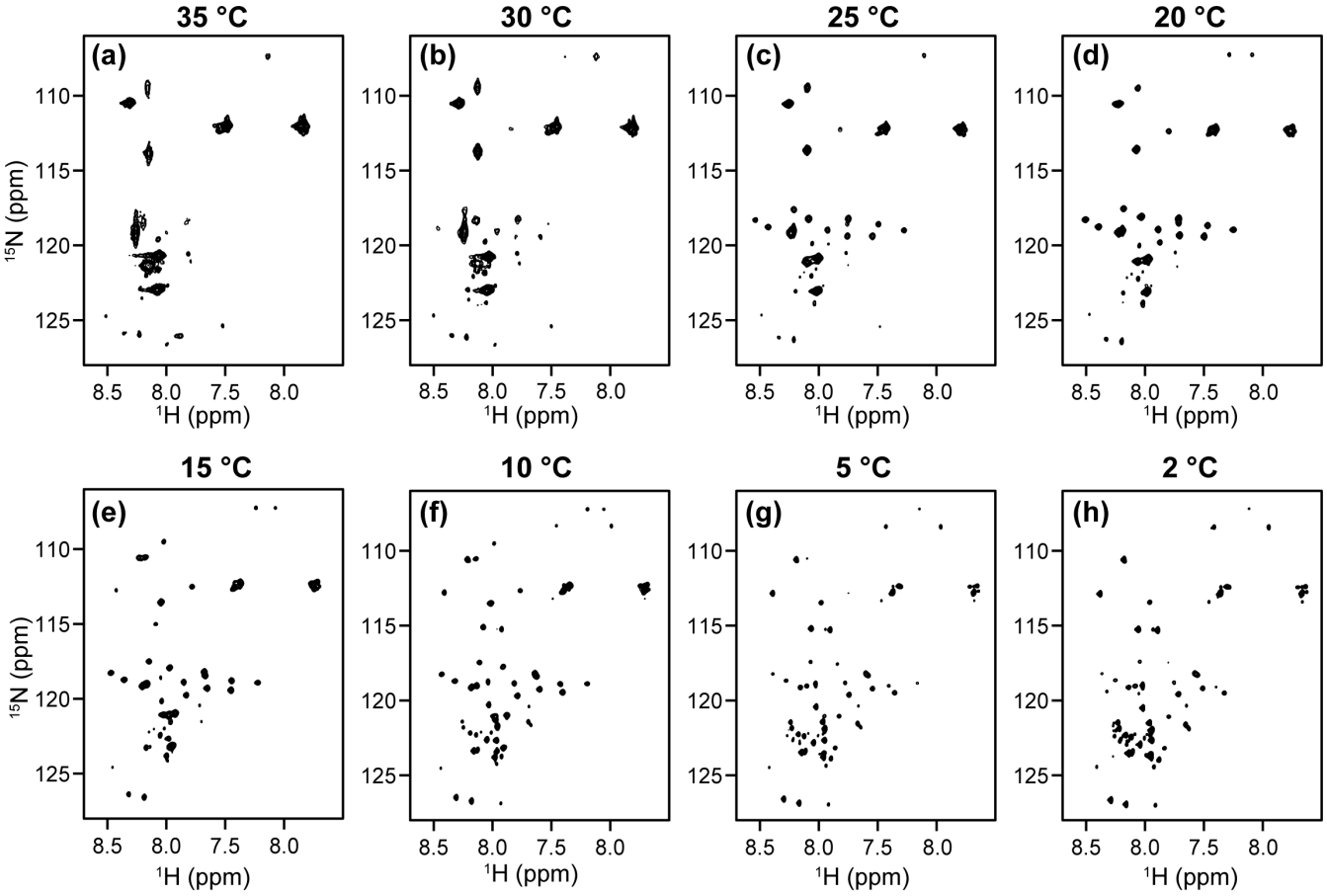

Figure S13. Temperature-dependent HSQC spectra of 1.0-mM ^{2}H,^{13}C,^{15}N-labeled melittin in 25-mM potassium phosphate, 50-mM NaCl, 3% D_2O on a 600-MHz spectrometer at atmospheric pressure. The temperature was decremented from 35 °C to 5 °C in 5 °C increments in (a)-(g), while the temperature was decremented by 3 °C in (h) to 2 °C to avoid freezing the sample. We note that even with C-terminal amidation, most of the tetrameric peaks are severely exchange-broadened above 20 °C and are undetectable at 35 °C. As the temperature is lowered, exchange broadening becomes less severe, but cold denaturation is observed; the relative fraction of unfolded peaks at atmospheric pressure goes up as the temperature is decreased. Each spectrum took 24 minutes to acquire for a total experimental time of 3.2 hours to collect these spectra, not including time spent equilibrating the temperature and reshimming the magnet.

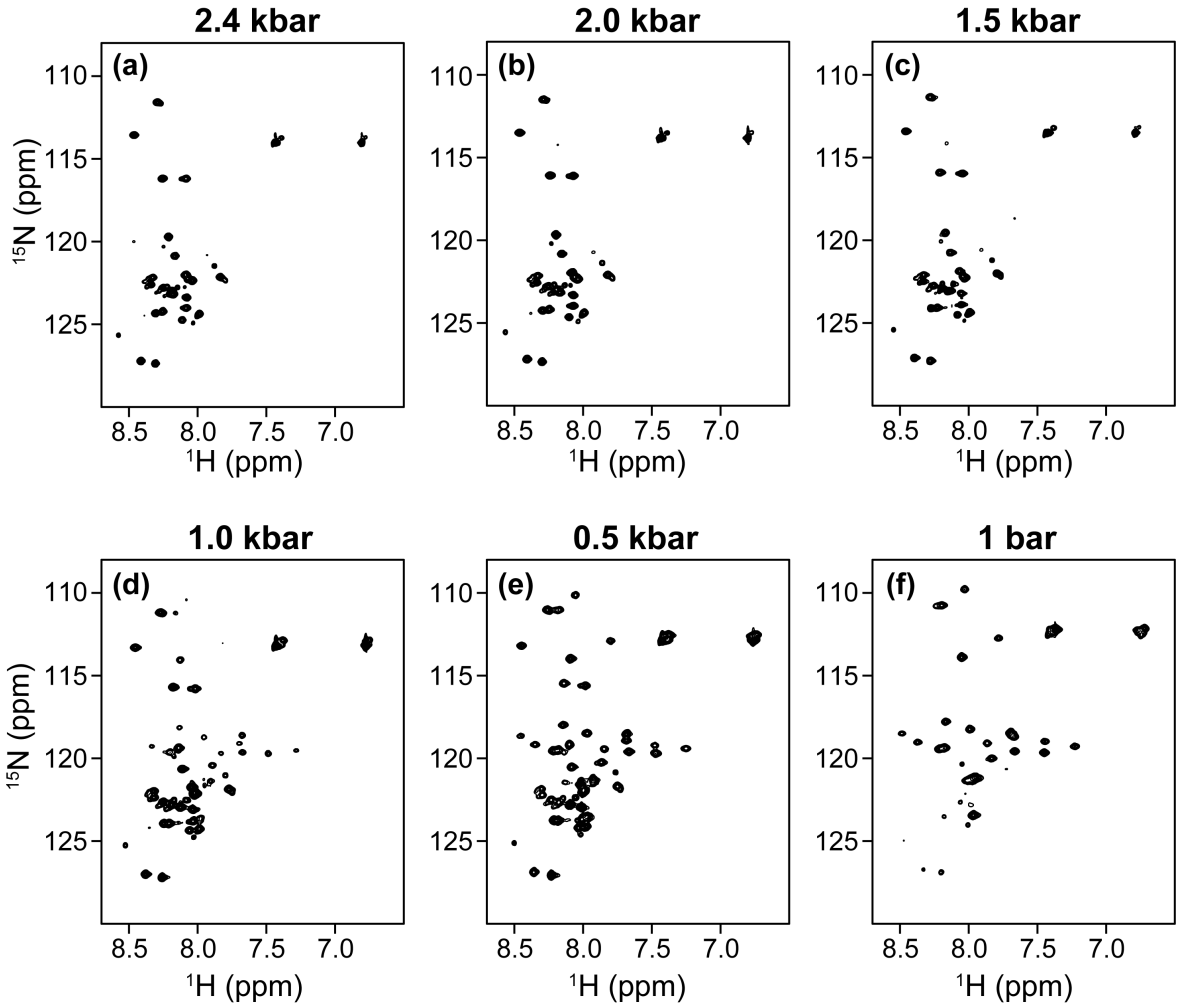

Figure S14. Pressure-dependent HSQC spectra of recombinantly expressed and chemically amidated ^{15}N-labeled melittin at 20 °C in 25-mM potassium phosphate pH 7.0, 50-mM NaCl, and 3% D_2O on a 600-MHz spectrometer. The pressure was decreased from (a) 2.4 kbar to (b) 2.0 kbar and then decremented in 0.5 kbar increments (b-f) until atmospheric pressure was reached. This sample was amidated with natural abundance NH_4Cl, and therefore the C-terminal amide is not visible in these spectra. At 500 bar, approximately half of the peptide is pressure-denatured and once the hydrostatic pressure is increased to 1.5 kbar, nearly all of the peptide is pressure-denatured. Each spectrum took 24 minutes to acquire for a total experimental time of 2.4 hours to collect these spectra, not including time spent equilibrating the temperature and reshimming the magnet.

Table S1. Amidated cationic membrane-lytic and antimicrobial peptides. There are myriad cationic membrane-lytic and antimicrobial peptides consisting of a C-terminal amidation post-translational modification that are of high interest to researchers and which our recombinant expression followed by chemical amidation could be immediately applied to. Below is a short representative list of such peptides.

Name	Sequence	Source	Reference
Indolicidin[50]	ILPWKWPWWPWRR-NH_2	Bovine neutrophils	Chan…Vogel, *Biochim. Biophys. Acta* **2006,** *1758***,** 1184-1202
PuroA[50]	FPVTWRWWKWWKG-NH_2	Wheat seeds	
$LfcinB_{4-9}$[50]	RRWQWR-NH_2	Fragment from bovine lactoferrin	
LysH[50]	RAWVAWR-NH_2	Fragment from human lysozyme	
PGLa[51]	GMASKAGAIAGKIAKV ALKAL-NH_2	*Xenopus laevis* (African clawed frog)	Hartmann…Ulrich, *Antimicrob. Agents Chemother*, **2010**, *54* (8), 3132-3142
LAH4[52]	KKALLALALHHLAHLALHLALA LKKA-NH_2	Designer synthetic peptide	Georgescu…Bechinger, *Biophys. J.* **2010**, *99* (8), 2507-2515.
Crabrolin[53]	FLPLILRKIVTAL-NH_2	European hornet venom	Krishnakumari…Nagaraj , *J. Pept. Res*. **1997**, *50* (2), 88-93.
Tachyplesin-1[54]	KWCFRVCYRGICYRRCR-NH_2	*Tachypleus tridentatus* (Japanese Horseshoe crab)	Edwards…Cooper, *ACS Infect. Dis.* **2017**, *3* (12), 917-926.
Temporin L[55]	FVQWFSKFLGRIL-NH_2	*Rana temporaria* (European red frog)	Mangoni…Rinaldi, *Biochem. J.* **2004**, *380*, 859-865.
Polyphemusin I[56]	RRWCFRVCYRGFCYRKCR-NH_2	*Limulus polyphemus* (American horseshoe crab)	Miyata…Shimonishi, J. Biochem. **1989**, *106*, 663-668.
Polyphemusin II[56]	RRWCFRVCYKGFCYRKCR-NH_2	*Limulus polyphemus* (American horseshoe crab)	
Tachyplesin II[56]	RWCFRVCYRGICYRKCR-NH_2	*Limulus polyphemus* (American horseshoe crab)	

Table S2. Melittin backbone chemical shifts (ppm). Deuterium isotope shift corrections were applied to all chemical shifts and pressure corrections were applied to the pressure denatured monomer chemical shifts. All shifts were measured on a 1.0-mM $^{2}H,^{13}C,^{15}N$-labeled melittin sample in 25-mM potassium phosphate buffer, pH 7.0, 50-mM NaCl, 3% D2O. The folded tetramer peaks were measured at atmospheric pressure, while the pressure denatured monomer resonances were measured at 2.25 kbar. These melittin backbone chemical shifts can be downloaded from https://doi.org/10.5281/zenodo.7574383. and have been deposited into the BMRB (BMRB 51703).

	Folded Tetramer				Pressure Denatured Monomer			
Residue	^{1}H	^{15}N	$^{13}C^{\alpha}$	$^{13}C'$	^{1}H	^{15}N	$^{13}C^{\alpha}$	$^{13}C'$
G1	-	-	-	-	-	-	43.23	170.51
I2	-	-	-	-	8.523	119.81	61.50	176.83
G3	-	-	-	-	8.578	112.75	45.02	173.60
A4			54.45	180.73	8.188	124.36	52.34	177.73
V5	7.613	118.96	65.03	177.72	8.219	120.67	62.29	176.11
L6	8.327	119.19	57.52	179.55	8.380	126.99	55.03	176.98
K7	7.811	119.44	58.22	179.25	8.378	123.87	56.14	176.16
V8	7.610	119.58	65.59	178.45	8.236	123.00	62.23	175.95
L9	8.131	118.03	57.23	177.46	8.486	126.82	55.05	177.56
T10	8.184	109.66	64.86	176.69	8.285	115.72	61.78	174.60
T11	7.950	112.69	63.56	176.57	8.117	115.71	61.77	174.89
G12	8.343	110.68	46.09	174.41	8.409	110.82	45.06	173.67
L13	8.188	121.22	58.89	-	8.161	123.14	53.57	-
P14	-	-	66.02	179.35	-	-	63.32	176.86
A15	7.389	119.06	54.40	180.68	8.328	123.76	52.61	177.93
L16	8.087	121.12	57.75	178.06	8.169	121.74	55.44	177.49
I17	8.522	118.88	64.97	178.09	8.139	122.04	61.37	176.54
S18	8.213	113.70	61.36	176.53	8.275	119.15	58.67	174.61
W19	8.114	123.30	62.14	178.34	8.148	123.51	58.22	176.53
I20	8.636	118.42	65.51	177.73	7.892	121.96	61.87	176.32
K21	8.312	117.64	59.66	179.35	8.061	123.98	56.91	176.82
R22	7.844	118.34	58.33	178.74	8.121	122.01	56.51	176.51
K23	8.017	119.02	56.06	179.12	8.271	122.59	56.65	176.89
R24	8.374	119.32	57.63	177.47	8.330	122.38	56.45	176.49
Q25	7.829	118.60	56.39	176.51	8.416	121.77	56.00	175.92
Q26	7.991	119.88	55.70	-	8.427	122.19	55.85	-

Table S3. Melittin experimental ^{15}N-^{1}H isotropic J-couplings, (J+$^{1}D_{NH}$) anisotropic couplings and $^{1}D_{NH}$ residual dipolar couplings. All couplings and errors are reported in Hz. Isotropic J-couplings were not measured for G3 and A4. In these cases, an average J-coupling of -93.3 Hz was used with an uncertainty of 1.1 Hz.[46] These couplings can be downloaded from https://doi.org/10.5281/zenodo.7574383. The RDCs have been deposited into the BMRB (BMRB 51703).

Residue	J	J_{err}	J+D_{Pf1}	(J+D_{Pf1}) err	$^{1}D_{NH,Pf1}$	$^{1}D_{NH,Pf1,err}$	J+$D_{,gel}$	(J+$D_{,gel}$) err	$^{1}D_{NH,gel}$	$^{1}D_{NH,gel,err}$
G3	-	-	-89.96	0.23	3.34	1.12	-	-	-	-
A4	-	-	-92.60	0.26	0.70	1.13	-94.12	0.59	-0.82	1.25
V5	-92.76	0.14	-80.83	0.17	11.92	0.22	-84.00	0.47	8.76	0.49
L6	-93.51	0.11	-84.31	0.13	9.20	0.17	-85.55	0.28	7.96	0.30
K7	-93.44	0.11	-93.67	0.21	-0.23	0.23	-92.30	0.40	1.14	0.42
V8	-93.34	0.11	-90.34	0.19	3.00	0.22	-92.25	0.38	1.09	0.40
L9	-93.30	0.16	-81.86	0.36	11.44	0.39	-85.02	0.57	8.28	0.60
T10	-92.51	0.26	-90.43	0.53	2.07	0.59	-88.74	0.67	3.77	0.72
T11	-92.72	0.25	-94.46	0.57	-1.73	0.62	-96.03	0.75	-3.31	0.80
G12	-93.71	0.15	-83.24	0.42	10.47	0.45	-86.63	0.30	7.08	0.33
L13	-93.61	0.15	-74.80	0.80	18.82	0.81	-80.88	0.46	12.73	0.48
P14	-	-	-	-	-	-	-	-	-	-
A15	-92.81	0.17	-83.88	0.60	8.93	0.62	-84.75	0.69	8.06	0.71
L16	-93.50	0.10	-75.80	0.27	17.71	0.29	-81.15	0.18	12.35	0.21
I17	-92.83	0.15	-80.94	0.30	11.89	0.34	-84.04	0.51	8.79	0.53
S18	-93.46	0.09	-86.66	0.14	6.79	0.17	-86.42	0.26	7.04	0.27
W19	-92.86	0.07	-79.18	0.30	13.68	0.31	-83.08	0.19	9.78	0.21
I20	-92.39	0.21	-75.58	0.50	16.81	0.55	-81.06	0.71	11.33	0.74
K21	-93.53	0.16	-83.56	0.46	9.97	0.48	-84.07	0.71	9.46	0.73
R22	-93.53	0.12	-86.67	0.30	6.86	0.32	-87.79	0.46	5.74	0.48
K23	-93.41	0.15	-78.53	0.32	14.88	0.35	-82.99	0.61	10.42	0.63
R24	-93.48	0.11	-83.76	0.46	9.73	0.48	-86.37	0.52	7.11	0.53
Q25	-92.76	0.14	-93.89	0.26	-1.13	0.29	-89.09	0.57	3.67	0.59
Q26	-92.66	0.13	-87.56	0.42	5.10	0.44	-88.74	0.65	3.92	0.66

Table S4. Analysis of the AlphaFold-Multimer structural models with respect to the melittin RDCs measured with the Pf1 alignment media. SVD fitting of the RDC alignment tensor parameters was done for residues 3-23 in the AF-M models and residues 3-25 in the 2MLT crystal structure. The AF-M model confidence score (confidence score = 0.8*ipTM + 0.2*pTM) is a prediction of the similarity between the AF-M model and the true oligomeric structure. The RMSD listed in the final column is the backbone RMSD between the AF-M structural models and the 2MLT X-ray crystal structure tetramer for residues 1-23.

Structure	Q factor	*Da* (Hz)	*Rh*	RMS (Hz)	Model Confidence	RMSD (Å)
2MLT	0.206	11.236	0.314	2.149	-	-
AF1	0.191	10.617	0.023	1.818	0.752	0.653
AF2	0.194	9.675	0.021	1.682	0.6818	0.889
AF3	0.17	-25.847	0.433	4.195	0.1514	9.73
AF4	0.633	6.324	0.237	3.653	0.14315	4.883
AF5	0.795	5.837	0.646	4.757	0.1314	6.884
AFD1	0.213	10.111	0.067	1.927	0.799	0.77
AFD2	0.189	10.15	0.049	1.717	0.7538	0.766
AFD3	0.189	10.58	0.042	1.787	0.7292	0.746
AFD4	0.213	10.576	0.059	2.017	0.5827	0.747
AFD5	0.375	11.926	0.026	3.997	0.4793	13.21
AFG1	0.207	10.473	0.043	1.945	0.7609	0.689
AFG2	0.162	10.242	0.017	1.482	0.7385	0.695
AFG3	0.165	9.272	0.085	1.369	0.6839	0.896
AFG4	0.191	10.087	0.132	1.731	0.5113	0.908
AFG5	0.431	10.974	0.133	4.263	0.321	12.898
AFK1	0.138	10.24	0.061	1.266	0.72212	0.677
AFK2	0.18	9.959	0.016	1.602	0.6969	0.769
AFK3	0.527	-11.153	0.315	5.447	0.1466	10.495
AFK4	0.599	6.587	0.086	3.541	0.1355	13.918
AFK5	0.433	-13.808	0.197	5.422	0.1349	8.039
AFR1	0.142	9.984	0.066	1.273	0.6917	0.745
AFR2	0.478	-10.669	0.011	4.559	0.1726	4.94
AFR3	0.826	5.725	0.061	4.233	0.1609	4.178
AFR4	0.221	-23.093	0.403	4.834	0.1487	8.032
AFR5	0.434	-11.383	0.091	4.432	0.1274	11.898

Table S5. Analysis of the AlphaFold-Multimer structural models with respect to the melittin RDCs measured with a stretched polyacrylamide gel alignment media. SVD fitting of the RDC alignment tensor parameters was done for residues 4-23 in the AF-M models and residues 4-25 in the 2MLT crystal structure. The AF-M model confidence score is a prediction of the similarity between the AF-M model and the true oligomeric structure. The RMSD listed in the final column is the backbone RMSD between the AF-M structural models and the 2MLT X-ray crystal structure tetramer for residues 1-23.

Structure	Q factor	*Da* (Hz)	*Rh*	RMS (Hz)	Model Confidence	RMSD (Å)
2MLT	0.307	7.547	0.368	2.176	-	-
AF1	0.209	7.444	0.31	1.443	0.752	0.653
AF2	0.173	7.081	0.36	1.15	0.6818	0.889
AF3	0.143	-20.071	0.406	2.722	0.1514	9.73
AF4	0.411	5.608	0.467	2.226	0.14315	4.883
AF5	0.515	5.566	0.48	2.779	0.1314	6.884
AFD1	0.187	7.221	0.415	1.281	0.799	0.77
AFD2	0.179	7.302	0.329	1.214	0.7538	0.766
AFD3	0.209	7.459	0.353	1.456	0.7292	0.746
AFD4	0.185	7.592	0.325	1.302	0.5827	0.747
AFD5	0.399	8.942	0.034	3.191	0.4793	13.21
AFG1	0.182	7.582	0.31	1.277	0.7609	0.689
AFG2	0.178	7.292	0.308	1.204	0.7385	0.695
AFG3	0.146	6.776	0.336	0.922	0.6839	0.896
AFG4	0.245	6.922	0.316	1.571	0.5113	0.908
AFG5	0.404	8.996	0.177	3.291	0.321	12.898
AFK1	0.174	7.273	0.282	1.167	0.72212	0.677
AFK2	0.166	7.245	0.316	1.113	0.6969	0.769
AFK3	0.431	-10.36	0.276	4.108	0.1466	10.495
AFK4	0.388	5.941	0.067	2.065	0.1355	13.918
AFK5	0.327	-12.056	0.158	3.555	0.1349	8.039
AFR1	0.163	7.133	0.333	1.083	0.6917	0.745
AFR2	0.48	-6.286	0.392	2.852	0.1726	4.94
AFR3	0.456	-5.361	0.636	2.497	0.1609	4.178
AFR4	0.177	-19.529	0.386	3.258	0.1487	8.032
AFR5	0.351	-8.924	0.173	2.834	0.1274	11.898

Table S6. RDC based ranking of melittin AlphaFold-Multimer structural models and the 2MLT crystal structure. Models are ranked according to the average Q factor in the two alignment media used in this study: Pf1 and a positively charged stretched polyacrylamide gel. The AF-M model confidence score is a prediction of the similarity between the AF-M model and the true oligomeric structure. The RMSD listed in the final column is the backbone RMSD between the AF-M structural models and the 2MLT X-ray crystal structure tetramer for residues 1-23.

Structure	$Q_{average}$	Q_{Pf1}	Q_{gel}	Model Confidence	RMSD (Å)
AFR1	0.153	0.142	0.163	0.692	0.745
AFG3	0.156	0.165	0.146	0.684	0.896
AFK1	0.156	0.138	0.174	0.722	0.677
AF3	0.157	0.170	0.143	0.151	9.730
AFG2	0.170	0.162	0.178	0.739	0.695
AFK2	0.173	0.180	0.166	0.697	0.769
AF2	0.184	0.194	0.173	0.682	0.889
AFD2	0.184	0.189	0.179	0.754	0.766
AFG1	0.195	0.207	0.182	0.761	0.689
AFD3	0.199	0.189	0.209	0.729	0.746
AFD4	0.199	0.213	0.185	0.583	0.747
AFR4	0.199	0.221	0.177	0.149	8.032
AF1	0.200	0.191	0.209	0.752	0.653
AFD1	0.200	0.213	0.187	0.799	0.770
AFG4	0.218	0.191	0.245	0.511	0.908
2MLT	0.258	0.209	0.306	-	-
AFK5	0.380	0.433	0.327	0.135	8.039
AFD5	0.387	0.375	0.399	0.479	13.210
AFR5	0.393	0.434	0.351	0.127	11.898
AFG5	0.418	0.431	0.404	0.321	12.898
AFK3	0.479	0.527	0.431	0.147	10.495
AFR2	0.479	0.478	0.480	0.173	4.940
AFK4	0.494	0.599	0.388	0.136	13.918
AF4	0.522	0.633	0.411	0.143	4.883
AFR3	0.641	0.826	0.456	0.161	4.178
AF5	0.655	0.795	0.515	0.131	6.884

Table S7. 2MLT crystal structure and AlphaFold-Multimer atomic coordinates. The X-ray crystal structure was retrieved from the protein data bank (PDB), then it was symmetry expanded into a tetramer, residues were renumbered as described in *3.3.3 Comparison of $^{1}D_{NH}$ couplings with the crystal structure and AlphaFold-Multimer model,* and finally protons were added to the structure with DYNAMO. The C-terminus column lists the C-terminal modifications for the AF-M structures in comparison to melittin's native -$CONH_2$ C-terminus. The atomic coordinates in the form of .pdb files can be downloaded from https://doi.org/10.5281/zenodo.7574383.

Structure	.pdb File	C-terminus
2MLT	2mlt.pdb	-$CONH_2$
AF1	af1.pdb	-COOH
AF2	af2.pdb	-COOH
AF3	af3.pdb	-COOH
AF4	af4.pdb	-COOH
AF5	af5.pdb	-COOH
AFD1	afd1.pdb	-D-COOH
AFD2	afd2.pdb	-D-COOH
AFD3	afd3.pdb	-D-COOH
AFD4	afd4.pdb	-D-COOH
AFD5	afd5.pdb	-D-COOH
AFG1	afg1.pdb	-G-COOH
AFG2	afg2.pdb	-G-COOH
AFG3	afg3.pdb	-G-COOH
AFG4	afg4.pdb	-G-COOH
AFG5	afg5.pdb	-G-COOH
AFK1	afk1.pdb	-K-COOH
AFK2	afk2.pdb	-K-COOH
AFK3	afk3.pdb	-K-COOH
AFK4	afk4.pdb	-K-COOH
AFK5	afk5.pdb	-K-COOH
AFR1	afr1.pdb	-R-COOH
AFR2	afr2.pdb	-R-COOH
AFR3	afr3.pdb	-R-COOH
AFR4	afr4.pdb	-R-COOH
AFR5	afr5.pdb	-R-COOH

References

(1) Ying, J.; Barnes, C. A.; Louis, J. M.; Bax, A. Importance of Time-Ordered Non-Uniform Sampling of Multi-Dimensional NMR Spectra of Aβ1–42 Peptide under Aggregating Conditions. *J. Biomol. NMR* **2019**, *73* (8–9), 429–441. https://doi.org/10.1007/s10858-019-00235-7.

(2) Butt, T. R.; Edavettal, S. C.; Hall, J. P.; Mattern, M. R. SUMO Fusion Technology for Difficult-to-Express Proteins. *Protein Expr. Purif.* **2005**, *43* (1), 1–9. https://doi.org/10.1016/j.pep.2005.03.016.

(3) Gelenter, M. D.; Mandala, V. S.; Niesen, M. J. M.; Sharon, D. A.; Dregni, A. J.; Willard, A. P.; Hong, M. Water Orientation and Dynamics in the Closed and Open Influenza B Virus M2 Proton Channels. *Commun. Biol.* **2021**, *4* (1), 1–14. https://doi.org/10.1038/s42003-021-01847-2.

(4) Zhou, L.; Liu, Z.; Xu, G.; Li, L.; Xuan, K.; Xu, Y.; Zhang, R. Expression of Melittin in Fusion with GST in Escherichia Coli and Its Purification as a Pure Peptide with Good Bacteriostatic Efficacy. *ACS Omega* **2020**, *5* (16), 9251–9258. https://doi.org/10.1021/acsomega.0c00085.

(5) Buhrman, J. S.; Rayahin, J. E.; Cook, L. C.; Federle, M. J.; Gemeinhart, R. A. Active, Soluble Recombinant Melittin Purified by Extracting Insoluble Lysate of Escherichia Coli without Denaturation. *Biotechnol. Prog.* **2013**, *29* (5), 1150–1157. https://doi.org/10.1002/btpr.1784.

(6) Rayahin, J. E.; Buhrman, J. S.; Gemeinhart, R. A. Melittin-Glutathione S-Transferase Fusion Protein Exhibits Anti-Inflammatory Properties and Minimal Toxicity. *Eur. J. Pharm. Sci. Off. J. Eur. Fed. Pharm. Sci.* **2014**, *65*, 112–121. https://doi.org/10.1016/j.ejps.2014.09.012.

(7) Shi, W.; Xu, H.; Cheng, J.; Zhang, C. Expression of the Melittin Gene of Apis Cerana Cerana in Escherichia Coli. *Protein Expr. Purif.* **2004**, *37* (1), 213–219. https://doi.org/10.1016/j.pep.2004.05.010.

(8) Raran-Kurussi, S.; Cherry, S.; Zhang, D.; Waugh, D. S. Removal of Affinity Tags with TEV Protease. In *Heterologous Gene Expression in E.coli: Methods and Protocols*; Burgess-Brown, N. A., Ed.; Methods in Molecular Biology; Springer: New York, NY, 2017; pp 221–230. https://doi.org/10.1007/978-1-4939-6887-9_14.

(9) Zou, X.; Liu, C.; Li, C.; Fu, R.; Xu, W.; Bian, H.; Dong, X.; Zhao, X.; Xu, Z.; Zhang, J.; Shen, Z. Study on the Structure-Activity Relationship of Dihydroartemisinin Derivatives: Discovery, Synthesis, and Biological Evaluation of Dihydroartemisinin-Bile Acid Conjugates as Potential Anticancer Agents. *Eur. J. Med. Chem.* **2021**, *225*, 113754. https://doi.org/10.1016/j.ejmech.2021.113754.

(10) Isidro-Llobet, A.; Álvarez, M.; Albericio, F. Amino Acid-Protecting Groups. *Chem. Rev.* **2009**, *109* (6), 2455–2504. https://doi.org/10.1021/cr800323s.

(11) Caro, J. A.; Wand, A. J. Practical Aspects of High-Pressure NMR Spectroscopy and Its Applications in Protein Biophysics and Structural Biology. *Methods* **2018**, *148*, 67–80. https://doi.org/10.1016/j.ymeth.2018.06.012.

(12) Lilja, H.; Weiber, H. Synthetic Protease Inhibitors and Post-Ejaculatory Degradation of Human Semen Proteins. *Scand. J. Clin. Lab. Invest.* **1984**, *44* (5), 433–438. https://doi.org/10.3109/00365518409083834.

(13) Hansen, M. R.; Mueller, L.; Pardi, A. Tunable Alignment of Macromolecules by Filamentous Phage Yields Dipolar Coupling Interactions. *Nat. Struct. Biol.* **1998**, *5* (12), 1065–1074. https://doi.org/10.1038/4176.

(14) Ruckert, M.; Otting, G. Alignment of Biological Macromolecules in Novel Nonionic Liquid Crystalline Media for NMR Experiments. *J. Am. Chem. Soc.* **2000**, *122* (32), 7793-7797. https://doi.org/10.1021/ja001068h.

(15) Maltsev, A. S.; Grishaev, A.; Roche, J.; Zasloff, M.; Bax, A. Improved Cross Validation of a Static Ubiquitin Structure Derived from High Precision Residual Dipolar Couplings Measured in a Drug-

Based Liquid Crystalline Phase. *J. Am. Chem. Soc.* **2014**, *136* (10), 3752-3755. https://doi.org/10.1021/ja4132642.

(16) Chou, J. J.; Gaemers, S.; Howder, B.; Louis, J.M.; Bax, A. A Simple Apparatus for Generating Stretched Polyacrylamide Gels, Yielding Uniform Alignment of Proteins and Detergent Micelles. *J. Biomol. NMR* **2001**, *21*, 377-382. https://doi.org/10.1023/A:1013336502594.

(17) Kay, L. E.; Ikura, M.; Tschudin, R.; Bax, A. Three-Dimensional Triple-Resonance NMR Spectroscopy of Isotopically Enriched Proteins. *J. Magn. Reson. 1969* **1990**, *89* (3), 496–514. https://doi.org/10.1016/0022-2364(90)90333-5.

(18) Charlier, C.; Alderson, T. R.; Courtney, J. M.; Ying, J.; Anfinrud, P.; Bax, A. Study of Protein Folding under Native Conditions by Rapidly Switching the Hydrostatic Pressure inside an NMR Sample Cell. *Proc. Natl. Acad. Sci.* **2018**, *115* (18), E4169–E4178. https://doi.org/10.1073/pnas.1803642115.

(19) Ying, J.; Chill, J. H.; Louis, J. M.; Bax, A. Mixed-Time Parallel Evolution in Multiple Quantum NMR Experiments: Sensitivity and Resolution Enhancement in Heteronuclear NMR. *J. Biomol. NMR* **2007**, *37* (3), 195–204. https://doi.org/10.1007/s10858-006-9120-z.

(20) Fitzkee, N. C.; Bax, A. Facile Measurement of 1H-15N Residual Dipolar Couplings in Larger Perdeuterated Proteins. *J. Biomol. NMR* **2010**, *48* (2), 65–70. https://doi.org/10.1007/s10858-010-9441-9.

(21) Ying, J.; Delaglio, F.; Torchia, D. A.; Bax, A. Sparse Multidimensional Iterative Lineshape-Enhanced (SMILE) Reconstruction of Both Non-Uniformly Sampled and Conventional NMR Data. *J. Biomol. NMR* **2017**, *68* (2), 101–118. https://doi.org/10.1007/s10858-016-0072-7.

(22) Delaglio, F.; Grzesiek, S.; Vuister, G. W.; Zhu, G.; Pfeifer, J.; Bax, A. NMRPipe: A Multidimensional Spectral Processing System Based on UNIX Pipes. *J. Biomol. NMR* **1995**, *6* (3), 277–293. https://doi.org/10.1007/BF00197809.

(23) Jumper, J.; Evans, R.; Pritzel, A.; Green, T.; Figurnov, M.; Ronneberger, O.; Tunyasuvunakool, K.; Bates, R.; Žídek, A.; Potapenko, A.; Bridgland, A.; Meyer, C.; Kohl, S. A. A.; Ballard, A. J.; Cowie, A.; Romera-Paredes, B.; Nikolov, S.; Jain, R.; Adler, J.; Back, T.; Petersen, S.; Reiman, D.; Clancy, E.; Zielinski, M.; Steinegger, M.; Pacholska, M.; Berghammer, T.; Bodenstein, S.; Silver, D.; Vinyals, O.; Senior, A. W.; Kavukcuoglu, K.; Kohli, P.; Hassabis, D. Highly Accurate Protein Structure Prediction with AlphaFold. *Nature* **2021**, *596* (7873), 583–589. https://doi.org/10.1038/s41586-021-03819-2.

(24) Evans, R.; O'Neill, M.; Pritzel, A.; Antropova, N.; Senior, A.; Green, T.; Žídek, A.; Bates, R.; Blackwell, S.; Yim, J.; Ronneberger, O.; Bodenstein, S.; Zielinski, M.; Bridgland, A.; Potapenko, A.; Cowie, A.; Tunyasuvunakool, K.; Jain, R.; Clancy, E.; Kohli, P.; Jumper, J.; Hassabis, D. Protein Complex Prediction with AlphaFold-Multimer. bioRxiv March 10, 2022, p 2021.10.04.463034. https://doi.org/10.1101/2021.10.04.463034.

(25) Robertson, A. J.; Courtney, J. M.; Shen, Y.; Ying, J.; Bax, A. Concordance of X-Ray and AlphaFold2 Models of SARS-CoV-2 Main Protease with Residual Dipolar Couplings Measured in Solution. *J. Am. Chem. Soc.* **2021**, *143* (46), 19306–19310. https://doi.org/10.1021/jacs.1c10588.

(26) Smith, T. F.; Waterman, M. S. Identification of Common Molecular Subsequences. *J. Mol. Biol.* **1981**, *147* (1), 195–197. https://doi.org/10.1016/0022-2836(81)90087-5.

(27) Henikoff, S.; Henikoff, J. G. Amino Acid Substitution Matrices from Protein Blocks. *Proc. Natl. Acad. Sci.* **1992**, *89* (22), 10915–10919. https://doi.org/10.1073/pnas.89.22.10915.

(28) Altschul, S. F.; Erickson, B. W. Optimal Sequence Alignment Using Affine Gap Costs. *Bull. Math. Biol.* **1986**, *48* (5), 603–616. https://doi.org/10.1016/S0092-8240(86)90010-8.

(29) Lee, W.; Tonelli, M.; Markley, J. L. NMRFAM-SPARKY: Enhanced Software for Biomolecular NMR Spectroscopy. *Bioinforma. Oxf. Engl.* **2015**, *31* (8), 1325–1327. https://doi.org/10.1093/bioinformatics/btu830.

(30) Koehler, J.; Beck Erlach, M.; Crusca, E.; Kremer, W.; Munte, C. E.; Kalbitzer, H. R. Pressure Dependence of 15N Chemical Shifts in Model Peptides Ac-Gly-Gly-X-Ala-NH2. *Materials* **2012**, *5* (10), 1774–1786. https://doi.org/10.3390/ma5101774.
(31) Erlach, M. B.; Koehler, J.; Crusca, E.; Kremer, W.; Munte, C. E.; Kalbitzer, H. R. Pressure Dependence of Backbone Chemical Shifts in the Model Peptides Ac-Gly-Gly-Xxx-Ala-NH2. *J. Biomol. NMR* **2016**, *65* (2), 65–77. https://doi.org/10.1007/s10858-016-0030-4.
(32) Maltsev, A. S.; Ying, J.; Bax, A. Deuterium Isotope Shifts for Backbone ^{1}H, ^{15}N and ^{13}C Nuclei in Intrinsically Disordered Protein α-Synuclein. *J. Biomol. NMR* **2012**, *54* (2), 181–191. https://doi.org/10.1007/s10858-012-9666-x.
(33) Anderson, D.; Terwilliger, T. C.; Wickner, W.; Eisenberg, D. Melittin Forms Crystals Which Are Suitable for High Resolution X-Ray Structural Analysis and Which Reveal a Molecular 2-Fold Axis of Symmetry. *J. Biol. Chem.* **1980**, *255* (6), 2578–2582. https://doi.org/10.1016/S0021-9258(19)85931-8.
(34) Terwilliger, T. C.; Eisenberg, D. The Structure of Melittin. I. Structure Determination and Partial Refinement. *J. Biol. Chem.* **1982**, *257* (11), 6010–6015. https://doi.org/10.1016/S0021-9258(20)65097-9.
(35) Terwilliger, T. C.; Eisenberg, D. The Structure of Melittin. II. Interpretation of the Structure. *J. Biol. Chem.* **1982**, *257* (11), 6016–6022. https://doi.org/10.1016/S0021-9258(20)65098-0.
(36) Schrödinger, LLC. The PyMOL Molecular Graphics System, Version 1.8, 2015.
(37) Losonczi, J. A.; Andrec, M.; Fischer, M. W. F.; Prestegard, J. H. Order Matrix Analysis of Residual Dipolar Couplings Using Singular Value Decomposition. *J. Magn. Reson.* **1999**, *138* (2), 334–342. https://doi.org/10.1006/jmre.1999.1754 .
(38) Saupe, A. Recent Results in the Field of Liquid Crystals. *Angew. Chem. Int. Ed. Engl.* **1968**, *7* (2), 97–112. https://doi.org/10.1002/anie.196800971.
(39) Chen, K.; Tjandra, N. The Use of Residual Dipolar Coupling in Studying Proteins by NMR. *Top. Curr. Chem.* **2012**, *326*, 47–67. https://doi.org/10.1007/128_2011_215.
(40) Clore, G. M.; Garrett, D. S. R-Factor, Free R, and Complete Cross-Validation for Dipolar Coupling Refinement of NMR Structures. *J. Am. Chem. Soc.* **1999**, *121* (39), 9008–9012. https://doi.org/10.1021/ja991789k.
(41) Prestegard, J. H.; Al-Hashimi, H. M.; Tolman, J. R. NMR Structures of Biomolecules Using Field Oriented Media and Residual Dipolar Couplings. *Q. Rev. Biophys.* **2000**, *33* (4), 371–424. https://doi.org/10.1017/S0033583500003656.
(42) Lorieau, J. L. Partial Alignment, Residual Dipolar Couplings and Molecular Symmetry in Solution NMR. *J. Biomol. NMR* **2019**, *73* (8–9), 477–491. https://doi.org/10.1007/s10858-019-00256-2.
(43) Ulmer, T. S.; Ramirez, B. E.; Delaglio, F.; Bax, A. Evaluation of Backbone Proton Positions and Dynamics in a Small Protein by Liquid Crystal NMR Spectroscopy. *J. Am. Chem. Soc.* **2003**, *125* (30), 9179–9191. https://doi.org/10.1021/ja0350684.
(44) Hornak, V.; Abel, R.; Okur, A.; Strockbine, B.; Roitberg, A.; Simmerling, C. Comparison of Multiple Amber Force Fields and Development of Improved Protein Backbone Parameters. *Proteins* **2006**, *65* (3), 712–725. https://doi.org/10.1002/prot.21123.
(45) Eastman, P.; Swails, J.; Chodera, J. D.; McGibbon, R. T.; Zhao, Y.; Beauchamp, K. A.; Wang, L.-P.; Simmonett, A. C.; Harrigan, M. P.; Stern, C. D.; Wiewiora, R. P.; Brooks, B. R.; Pande, V. S. OpenMM 7: Rapid Development of High Performance Algorithms for Molecular Dynamics. *PLOS Comput. Biol.* **2017**, *13* (7), e1005659. https://doi.org/10.1371/journal.pcbi.1005659.
(46) Xu, J.; Zhang, Y. How Significant is a Protein Structure Similarity with TM-Score = 0.5? *Bioinformatics* **2010**, *26* (7), 889-895. https://doi.org/10.1093/bioinformatics/btq066.

(47) Chiliveri, S. C.; Robertson, A. J.; Shen, Y.; Torchia, D. A.; Bax, A. Advances in NMR Spectroscopy of Weakly Aligned Biomolecular Systems. *Chem. Rev.* **2022**, *122* (10), 9307–9330. https://doi.org/10.1021/acs.chemrev.1c00730.

(48) Shen, Y.; Bax, A. Protein Backbone and Sidechain Torsion Angles Predicted from NMR Chemical Shifts Using Artificial Neural Networks. *J. Biomol. NMR* **2013**, *56* (3), 227–241. https://doi.org/10.1007/s10858-013-9741-y.

(49) Kjaergaard, M.; Poulsen, F. M. Sequence Correction of Random Coil Chemical Shifts: Correlation between Neighbor Correction Factors and Changes in the Ramachandran Distribution. *J. Biomol. NMR* **2011**, *50* (2), 157–165. https://doi.org/10.1007/s10858-011-9508-2.

(50) Chan, D. I.; Prenner, E. J.; Vogel, H. J. Tryptophan- and Arginine-Rich Antimicrobial Peptides: Structures and Mechanisms of Action. *Biochim. Biophys. Acta.* **2006**, *1758* (9), 1184-1202. https://doi.org/10.1016/j.bbamem.2006.04.006.

(51) Hartmann, M.; Berditsch, M.; Hawecker, J.; Ardakana, M. F.; Gerthsen, D.; Ulrich, A. S. Damage of the Bacterial Cell Envelope by Antimicrobial Peptides Gramicidin S and PGLa as Revealed by Transmission and Scanning Electron Microscopy. *Antimicrob. Agents Chemother.* **2010**,*54* (8), 3132–3142. https://doi.org/10.1128/aac.00124-10.

(52) Georgescu, J.; Munhoz, V. H. O.; Bechinger, B. NMR Structures of the Histidine-Rich Peptide LAH4 in Micellar Environments: Membrane Insertion, pH-Dependent Mode of Antimicrobial Action, and DNA Transfection. *Biophys. J.* **2010**, *99* (8), 2507-2515. https://doi.org/10.1016%2Fj.bpj.2010.05.038.

(53) Krishnakumari, V.; Nagaraj. Antimicrobial and Hemolytic Activities of Crabrolin, a 13-Residue Peptide from the Venom of the European Hornet, Vespa Crabro, and its Analogs. *J. Pept. Res.* **1997**, *50* (2), 88-93. https://doi.org/10.1111/j.1399-3011.1997.tb01173.x.

(54) Edwards, I. A.; Elliot, A. G.; Kavanagh, A. M.; Blaskovich, M. A. T.; Cooper, M. A. Structure-Activity and -Toxicity Relationships of the Antimicrobial Peptide Tachyplesin-1. *ACS Infect. Dis.* **2017**, *3* (12), 917-926. https://doi.org/10.1021/acsinfecdis.7b00123.

(55) Mangoni, M. L.; Papo, N.; Barra, D.; Simmaco, M.; Bozzi, A.; Di Giulio, A.; Rinaldi, A. C. Effects of the Antimicrobial Peptide Temporin L on Cell Morphology, Membrane Permeability, and Viability of Eschericchia coli. *Biochem. J.* **2004**, *380*, 859-865. https://doi.org/10.1042%2FBJ20031975.

(56) Miyata, T.; Tokunaga, F.; Yoneya, T.; Yoshikawa, K.; Iwanaga, S.; Niwa, M.; Takao, T.; Shimonishi, Y. Antimicrobial Peptides, Isolated from Horseshoe Crab Hemocytes, Tachyplesin II, and Polyphemusins I and II: Chemical Structures and Biological Activity. *J. Biochem.* **1989**, *106*, 663-668. https://doi.org/10.1093/oxfordjournals.jbchem.a122913.